C h a p t e r   4

DIAGENETIC STABILIZATION OF MANGANESE-RICH SEDIMENTARY ROCKS

Kyle S. Metcalfe[1], Jena E. Johnson[2], Samuel M. Webb[3], Woodward W. Fischer[1]

[1] Division of Geological and Planetary Sciences,
California Institute of Technology, Pasadena, California, 91125

[2] Department of Earth and Environmental Sciences,
University of Michigan, Ann Arbor, MI 48109

[3] Stanford Synchrotron Radiation Lightsource,
Stanford University, Menlo Park, CA 94025

ABSTRACT

Precambrian manganese-rich sedimentary rocks comprise prominent portions of the rock record spanning periods of dramatic environmental change, but the imprint of early diagenesis on these deposits partially obscures the processes that produced the primary Mn-rich sediments. We constructed a numerical model simulating early diagenesis of mixed Fe-Mn sediments to ascertain the environmental and geobiological parameters that are important for the diagenetic stabilization of Mn-rich sedimentary rocks. We constrained our model with a case study presented by the vast, classic Mn deposits of Kalahari Manganese Field hosted by the Paleoproterozoic-age Hotazel Formation in the Transvaal Supergroup, South Africa, the largest known Mn deposits in the geological record. We benchmarked model results using synchrotron X-ray fluorescence spectroscopy imaging of the composition and Mn redox states of a sample of iron- and manganese-rich strata of the Hotazel Formation. We found that our model could produce a mineral assemblage

comparable to that of the Hotazel Formation, defined by Mn^{3+} : Mn^{2+} and Fe : Mn ratios. These results demonstrated that the Mn(III)-rich mineralogy of the Hotazel Formation required a significant flux reducing potential, provided by organic carbon, to produce concentrations of $Mn^{2+}_{(aq)}$ sufficient to overcome the thermodynamic threshold for reaction with solid-phase $Mn^{4+}O_2$ and resulting $Mn^{3+}OOH$ precipitation. When the rate constant for metal reduction in our model was reduced by 5-6 orders of magnitude, representing the delivery rate of abiotic reductants, Mn(III) phases were not observed, indicating that for this system, biological catalysis was necessary to produce the abundant Mn(III) phases observed in the Hotazel Formation. These modeling results led us to speculate that the Mn- and Fe-rich strata in the Hotazel Formation reflect deposition of a significant amount of organic carbon contemporaneously with metal oxides in a basin where deposited MnO_2 : $Fe^{3+}OOH$ ratios were determined by changes in the transportation of water masses through a basin in direct communication with high-potential oxidants like those provided by photosystem II or atmospheric O_2.

INTRODUCTION

The history recorded by Precambrian Mn-rich sedimentary rocks is challenging to decipher due to a lack of analogous modern sediments. Although some modern sedimentary environments have produced Mn nodules dispersed on the seafloor (Margolis and Burns, 1976; Post, 1999; Glasby, 2006), modern basins lack thick deposits of Mn-rich sediments such as those produced by some basins of Paleoproterozoic age that contain as much as ~2.7 x 10^{15} g Mn (Gutzmer and Beukes, 1996; Cairncross and Beukes, 2013). Explaining the petrogenesis of Mn-rich sedimentary rocks requires mechanisms that concentrated Mn sufficiently in a water body to produce large volumes of Mn-rich sediments. Mn is present in the crust is typically divalent, producing soluble Mn^{2+} upon dissolution of the original igneous or metamorphic mineral hosts of these metals (Calvert and Pedersen, 1996; Post, 1999). Mn^{2+} is highly soluble, and if not oxidized will be slowly sequestered in carbonate phases at concentrations proportional to its dissolved concentration (Holland, 1984; Mucci, 2004; Johnson et al., 2013; Fischer et al., 2016). Mn concentrations in carbonates indicate seawater Mn concentrations have remained between seven to two orders of magnitude lower than $Ca^{2+}_{(aq)}$ concentrations throughout Earth history (Fischer et al., 2016), demonstrating that a mechanism to concentrate Mn is necessary to produce the Mn-rich carbonates common in Mn-rich sedimentary rocks (Holland, 1984; Veizer et al., 1989; Johnson et al., 2016b; Lingappa et al., 2019).

Prior studies have focused on oxidation and sedimentation of insoluble oxide particles as the primary mechanism of Mn concentration for Mn-rich sediments. In modern environments, Mn is concentrated by oxidation of dissolved Mn^{2+} to insoluble Mn(III) or

Mn(IV) phases, which settle from suspension as particles or accumulate as nodules at the sediment-water interface (Margolis and Burns, 1976; Post, 1999; Glasby, 2006). As oxidation of $Mn^{2+}_{(aq)}$ is crucial for the precipitation and sedimentation of Mn-rich minerals in modern environments, it has been inferred as the process by which Precambrian Mn-rich sediments were emplaced (Johnson et al., 2013, 2016b). Importantly for paleobiological interpretations of Mn-rich sediments, the high redox potential of Mn necessitates either the presence of significant concentrations of O_2 or specialized biochemistry (Johnson et al., 2013) to oxidize $Mn^{2+}_{(aq)}$ and produce Mn-rich sedimentary rocks. The temporal distribution of Mn-rich sedimentary rocks, reaching a maximum in the Paleoproterozoic, has been explained by invoking the evolution of a Mn-oxidizing photosystem (Johnson et al., 2013) as well as oxidation of Mn- and Fe-rich seawater by free O_2 to form large deposits (Beukes, 1983, 1987; Kirschvink et al., 2000; Tsikos et al., 2003; Kopp et al., 2005; Hoffman, 2013).

Although the precursor Mn phases to those observed in Precambrian Mn-rich sedimentary rocks were oxides, these phases are often found in these rocks as Mn(II)- and/or Mn(III)-bearing minerals (Johnson et al., 2016b), implying that primary Mn oxides were subjected to syn- or post-depositional reduction. Examples of these deposits can be found throughout the Precambrian rock record (Johnson et al., 2016b), including the Hotazel Formation of northern South Africa, a massive Late Archaean-Early Paleoproterozoic deposit containing abundant braunite [$Mn^{2+}Mn^{3+}_6SiO_{12}$] and kutnohorite [$CaMn^{2+}(CO_3)_2$] (Schneiderhan et al., 2006; Johnson et al., 2016b), as well as the Neoproterozoic Santa Cruz Formation of southern Brazil, composed of braunite and rhodochrosite [$Mn^{2+}CO_3$] in well-preserved sections (Johnson et al., 2016b). The process responsible for the stabilization of Mn(III)-bearing minerals such as braunite in Precambrian Mn-rich sedimentary rocks represents a particularly interesting gap in our current understanding of the petrogenesis of these rocks. Braunite has been hypothesized to form during late diagenesis from reaction of a Mn(III) oxyhydroxide/oxide precursors such as bixbyite [α-$Mn^{3+}{}_2O_3$] with silica (Robie et al., 1995; Johnson et al., 2016b), but the conditions leading to the initial stabilization of the Mn(III) oxyhydroxide or Mn(III) oxide precursor are poorly understood.

To investigate the history recorded by Mn(III)-bearing minerals in Precambrian Mn-rich sedimentary rocks, we must first identify whether their Mn(III) precursor phases were the product of early diagenesis or later alteration. Study of the texture and redox states of Mn and Fe minerals in Mn-rich deposits has indicated that these precursor phases to these minerals were the products of early diagenetic processing: facies often contain well-preserved early diagenetic textures, including fine-grained crystals of Mn carbonates and braunite that delineate bedding (Johnson et al., 2016b). Other early diagenetic textures include abundant mm-scale Mn-bearing carbonate nodules that reflect early preferential cementation, where CO_3^{2-} and $Mn^{2+}{}_{(aq)}$ and $Ca^{2+}{}_{(aq)}$ were of sufficient concentrations to precipitate Mn-rich carbonate minerals (Mucci, 2004; Johnson et al., 2016b). Some Mn-rich sedimentary deposits contain crystals of Mn carbonates with Ca- and Mn-rich zones that vary in composition from kutnohorite [$CaMn^{2+}(CO_3)_2$] to Ca-rich rhodochrosite [$Mn^{2+}CO_3$], indicating dynamic geochemical conditions during syn- and/or post-depositional precipitation of these phases from a fluid of time-varying composition

(Schneiderhan et al., 2006; Johnson et al., 2016b). Mn carbonates are found intergrown with Mn(III) minerals including braunite in textures that imply formation of the precursor Mn(III) phase contemporaneous to Mn carbonate precipitation (Nel et al., 1986; Schneiderhan et al., 2006; Johnson et al., 2016b). $\delta^{13}C$ measurements of Mn carbonates document light values (–8.3 to –12.5‰), reflecting the imprint of early diagenesis driven by organic carbon oxidation on these phases (Okita et al., 1988; Tsikos et al., 2003; Maynard, 2010). Organic carbon oxidation coupled to metal reduction by microorganisms has been inferred as a reductive process primarily responsible for the production of $Mn^{2+}_{(aq)}$ available for precipitation as carbonate minerals (Schneiderhan et al., 2006; Johnson et al., 2016b). $Fe^{2+}_{(aq)}$ has also been implicated as a major electron donor for abiotic reduction of sedimentary Mn oxides (Postma, 1985; Van Cappellen and Wang, 1996; Postma and Appelo, 2000), and was likely important for the early diagenesis of Mn-rich sediments given the abundance of hematite [$Fe^{3+}_2O_3$] intergrown with Mn carbonate phases observed in the Hotazel Formation (Schneiderhan et al., 2006). The pervasive imprint of early diagenetic processes on Mn-rich sedimentary rocks thus enables interpretation of the mineral assemblages observed in these formations as reflective of the biogeochemical environment at or near to the time of deposition.

With the relative timing of the precipitation of Mn(III) oxyhydroxides/oxides in Mn-rich sediments constrained to early diagenesis, the processes potentially responsible for the stabilization of these phases can then be identified. Dissolved and solid-phase Mn^{3+} species can be generated as a transient intermediate during microbial reduction of Mn oxides (Kostka et al., 1995; Lin et al., 2012; Madison et al., 2013) or microbial oxidation of

Mn(II) (Webb et al., 2005), and in larger quantities by reaction of $Mn^{2+}_{(aq)}$ with Mn(IV) oxides, a comproportionation reaction thermodynamically favorable at pH > 7 (Elzinga, 2011; Takashima et al., 2012; Lefkowitz et al., 2013; Johnson et al., 2016a):

$$4H^+ + Mn^{2+}_{(aq)} + MnO_2 \Rightarrow 2Mn^{3+} + 2H_2O \tag{1}$$

Mn^{3+} produced by either pathway may be stabilized by ligand complexes (Duckworth and Sposito, 2005; Madison et al., 2013; Oldham et al., 2015) or by the precipitation of Mn(III) oxyhydroxides/oxides (Elzinga, 2011), the latter being ultimately a necessary requirement to generate Mn(III) minerals. Experimental precipitation of Mn(III) oxyhydroxides/oxides carried out under conditions relevant to the early diagenesis of Mn-rich sediments typically produces a metastable feitknechtite [β-MnOOH], which quickly stabilizes as manganite [γ-MnOOH] (Hem and Lind, 1983; Elzinga, 2011; Lefkowitz et al., 2013; Elzinga and Kustka, 2015) or hausmannite [Mn_3O_4] (Lefkowitz et al., 2013), depending on solution pH and composition. The synthesis route for braunite from Mn(III) precursor phases such as manganite or hausmannite remains uncertain, however. While manganite can be readily dehydrated to γ-Mn_2O_3 by heating to 200-250 ˚C under anoxic conditions (Hernan et al., 1986), the synthesis of bixbyite [α-Mn_2O_3] from manganite is unclear but may require the presence of Fe^{3+} during manganite dehydration, as Fe^{3+} is known to stabilize the bixbyite crystal structure (Waychunas, 1991).

In addition to the comproportionation reaction between Mn^{2+} and Mn(IV) oxides, we can identify three important processes involved in syn- and post-depositional modification of Mn-rich sediments that determine the stability of Mn(III) oxyhydroxide/oxide precipitates, including 1) reduction of metal oxides by oxidation of co-sedimentary organic carbon, 2) precipitation of carbonates as cements and nodules, and 3) reduction of Mn oxides by dissolved Fe^{2+}:

1. The microbial oxidation of organic carbon provides electrons to reduce primary Mn- and Fe-oxides and consumes H^+, according to equations 2 through 4 below, using formaldehyde to substitute for a complex set of organic carbon compounds that could serve as electron donors for metal reduction:

$$2MnO_{2\,(s)} + CH_2O + 4H^+ => 2Mn^{2+}{}_{(aq)} + CO_2 + 3H_2O \quad (2)$$

$$4MnOOH_{(s)} + CH_2O + 8H^+ => 4Mn^{2+}{}_{(aq)} + CO_2 + 7H_2O \quad (3)$$

$$4FeOOH_{(s)} + CH_2O + 8H^+ => 4Fe^{2+}{}_{(aq)} + CO_2 + 7H_2O \quad (4)$$

Microbial communities present in sediments are known to play a fundamental role in governing the rate, degree, and character of organic carbon oxidation; thus, to understand the stabilization of Mn(III) oxyhydroxide/oxide precipitates, the process and products of microbial metal reduction must be addressed (Froelich et al., 1979; Van Cappellen and Wang, 1996). Eq. 2 assumes MnO_2 reduction via a pathway that simultaneously transfers two e^- to MnO_2 from organic carbon, which has been documented by the model metal-reducing microorganism *Shewanella oneidensis* MR-1 (Kotloski and Gralnick, 2013; Johnson et al., 2016a). One-electron pathways of Mn(IV) oxide reduction have also been observed that produce small concentrations of Mn^{3+} intermediates relative to Mn^{2+} (Kostka et al., 1995; Lin et al., 2012), but the dominant products of microbial Mn- and Fe-oxide reduction are dissolved Mn^{2+} and Fe^{2+} (Froelich et al., 1979; Myers and Nealson, 1988; Lovley, 1991; Van Cappellen and Wang, 1996). $Mn^{2+}_{(aq)}$ produced from microbial respiration of Mn oxides can then react with Mn(IV) oxides to produce Mn(III) oxyhydroxide/oxide phases (Eq. 1), facilitated by the pH increase driven by Mn oxide reduction.

2. As shown in Eqs. 2-4, microbial metal reduction consumes H^+ and produces inorganic carbon. This in turn increases alkalinity and pH, and catalyzes the precipitation of carbonate cements and nodules (Raiswell and Fisher, 2000):

$$CO_3^{2-}{}_{(aq)} + M^{2+}{}_{(aq)} \Rightarrow MCO_{3\,(s)} \qquad (5)$$

where M^{2+} can be Ca^{2+}, Mg^{2+}, Mn^{2+}, or Fe^{2+}, depending on solution composition. In Mn-rich sedimentary rocks, observed carbonates include kutnohorite, Mn-rich calcites, ankerite [$Ca(Fe^{2+},Mn^{2+},Mg)(CO_3)_2$] and rarely siderite [$Fe^{2+}CO_3$] (Nel et al., 1986; Maynard, 2010; Johnson et al., 2016b). Precipitation of Mn carbonates consumes $Mn^{2+}_{(aq)}$ otherwise available for reaction with Mn(IV) oxides, and thus is in direct competition for $Mn^{2+}_{(aq)}$ with the $Mn^{2+} – Mn^{4+}$ comproportionation reaction (Eq. 1). However, the kinetics of these processes are significantly different, as Mn carbonate precipitation occurs significantly more slowly than $Mn^{2+} – Mn^{4+}$ comproportionation (Johnson et al., 2016a), but requires significantly lower $Mn^{2+}_{(aq)}$ concentrations to be thermodynamically favorable (Jensen et al., 2002; Lefkowitz et al., 2013).

3. Reactions between Mn and Fe constitute a third process important in early diagenetic processing of Mn-rich sediments (Postma, 1985; Van Cappellen and

Wang, 1996; Postma and Appelo, 2000). $Fe^{2+}_{(aq)}$ can reduce Mn(IV) phases forming a range surface-bound Fe oxide phases depending on solution composition (Schaefer et al., 2017):

$$2H_2O + 2Fe^{2+}_{(aq)} + MnO_2 \Rightarrow 2FeOOH_{(s)} + 2H^+ + Mn^{2+}_{(aq)} \qquad (6)$$

This reaction is known to be rapid (Siebecker et al., 2015; Johnson et al., 2016a) but self-limiting, due to the accumulation of Fe oxides that occlude reactive sites on the Mn oxide surface, preventing further reaction with $Fe^{2+}_{(aq)}$ (Villinski et al., 2001, 2003). This process is particularly interesting in the context of the early diagenesis of Mn-rich sediments, as it couples anaerobic Fe oxidation to production of $Mn^{2+}_{(aq)}$ and protons. While the production of $Mn^{2+}_{(aq)}$ from anaerobic Fe oxidation will increase the favorability of Mn(III) oxyhydroxide/oxide precipitation, concomitant acid production will decrease the favorability of this reaction.

Understanding the impact of these intertwined processes on the stability of Mn(III) oxyhydroxides/oxides requires an evaluation of the kinetics of these chemical reaction, which often compete for reactants or couple redox cycling to alkalinity changes in complex and sometimes self-limiting ways. To account for these interactions and to interpret the geochemical conditions responsible for the stabilization of Mn(III) precursor phases in the rock record, we constructed a numerical model simulating the products of early diagenesis for a range of initial compositions of the primary sediments, varying proportions of organic carbon, Mn oxides, and Fe oxides. We then compared the model outputs to a case study of the Hotazel Formation to constrain the initial sediment composition that stabilized Mn(III) phases in primary sediments of this Mn-rich deposit.

GEOLOGICAL BACKGROUND OF HOTAZEL CASE STUDY

Stratigraphically, the Hotazel Formation is a part of the Late Archaean-Early Paleoproterozoic Transvaal Supergroup (Fig. 1a), a thick package of predominantly well-preserved (Gutzmer and Beukes, 1996; Tsikos et al., 2003, 2010) sedimentary and minor volcanic rocks providing one of few windows into biogeochemistry across a unique interval of Earth history (Beukes, 1987; Condie, 1993; Knoll and Beukes, 2009; Hoffman, 2013; Johnson et al., 2013). Within the Transvaal Supergroup, the Hotazel is a part of the Postmasburg Group, a conformable sequence of glacial, volcanic, and Mn-rich deposits outcropping in western outcrops of the Transvaal Supergroup known as the Griqualand West Basin. The Hotazel Formation is conformably underlain by the volcanic Ongeluk Formation (Schneiderhan et al., 2006), which is in turn conformably underlain by the glaciogenic Makganyene Formation (Evans et al., 1997). In some interpretations, the Makganyene Formation has been correlated to a disconformity within the Duitschland and Rooihoogte formations in eastern outcrops of the Transvaal Supergroup known as the Eastern Transvaal Basin (Guo et al., 2009; Hoffman, 2013; Luo et al., 2016). In other interpretations, the Ongeluk Formation and therefore the underlying Makganyene Formation are significantly older and roughly contemporaneous with carbonates of the Chuniespoort Group in the Eastern Transvaal Basin (Gumsley et al., 2017). In all models, the Hotazel Formation postdates evidence for the first accumulation of atmospheric O_2 in

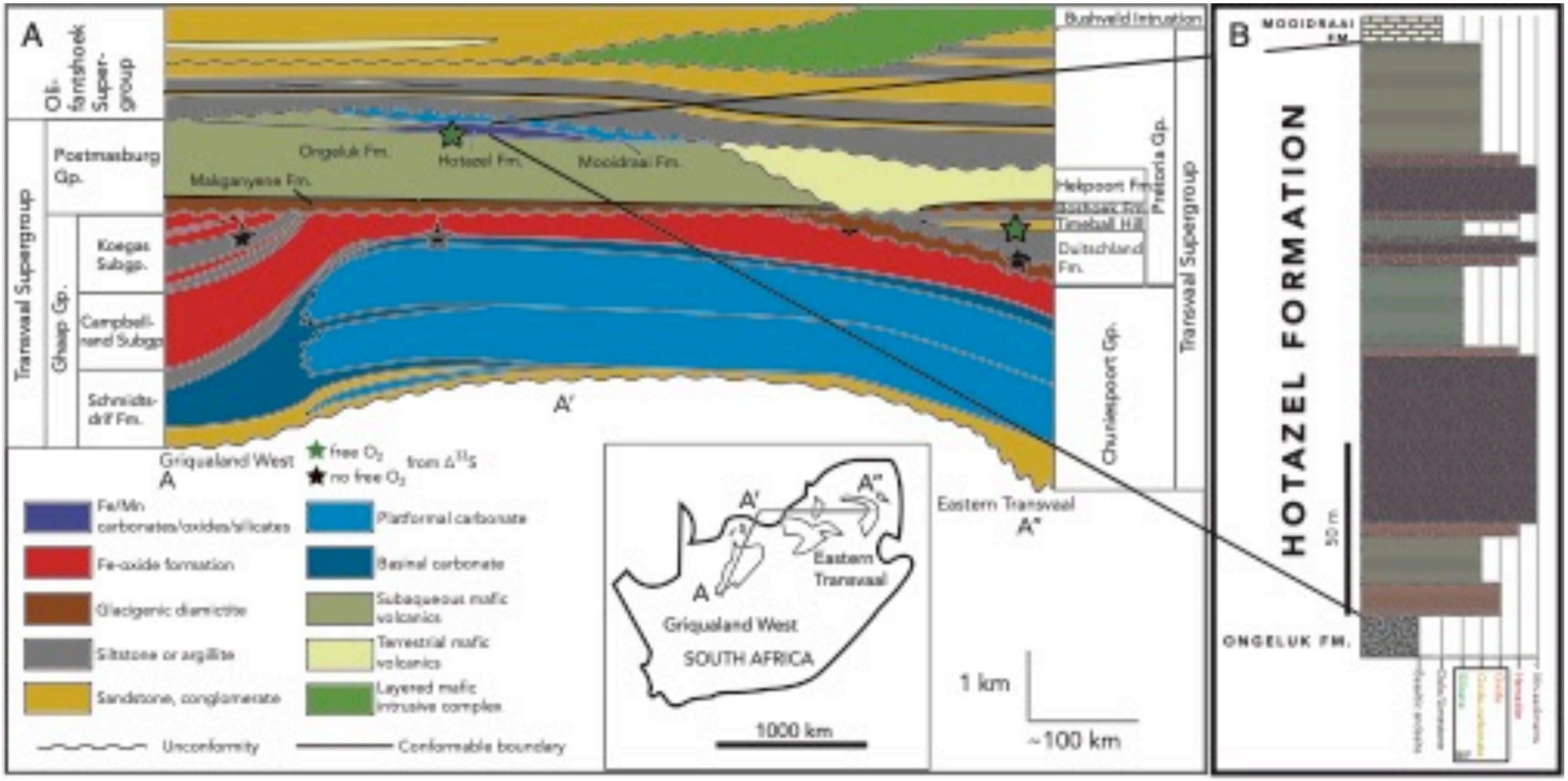

Figure 1.—Summary of the geological context of the Hotazel Formation. **A**) Composite stratigraphy of the Transvaal Supergroup, (after (Beukes, 1983), modified by correlations of (Hoffman, 2013; Luo, Ono, Beukes, Wang, Xie and Summons, 2016)). **B**) Stratigraphy of the Hotazel Formation from a drill core (after (Schneiderhan, Gutzmer, Strauss, Mezger and Beukes, 2006)).

samples of the Transvaal Supergroup from the Eastern Transvaal Basin (Farquhar et al. 2000; Bekker et al., 2001; Guo et al., 2009; Hoffman, 2013; Luo et al., 2016; Gumsley et al., 2017), and thus records an interval of profound change in the Earth system.

Given that the Hotazel Formation was deposited during one of the most dynamic periods of Earth history, several researchers have sought to examine the petrogenesis of these unique Mn-rich sedimentary rocks. That the Hotazel Formation conformably overlies the glaciogenic Makganyene Formation has led to the interpretation that the Hotazel was deposited from oxidation of a water column rich in $Mn^{2+}_{(aq)}$ and $Fe^{2+}_{(aq)}$ that was isolated from atmospheric O_2 by a global glaciation (Beukes, 1983; Kirschvink et al., 2000; Kopp et al., 2005; Schneiderhan et al., 2006). Cornell and Schutte alternatively suggested an alternative model in which the Hotazel Formation was a volcanogenic exhalative deposit related to Ongeluk volcanism (Cornell and Schütte, 1995). However, the presence of multiple paleomagnetic poles recorded by hematite in the Hotazel Formation has contradicted this hypothesis, supporting instead an origin from sedimentation of primary metal oxides precipitated from seawater (Evans et al., 2001). In this study, we use the petrogenetic framework for the deposition of the Hotazel wherein primary Fe and Mn oxides sediments were generated from oxidation of seawater $Mn^{2+}_{(aq)}$ and $Fe^{2+}_{(aq)}$ (Schneiderhan et al., 2006; Johnson et al., 2016b), and further consider the early diagenesis and kinetic constraints on the deposition of the Hotazel Formation.

The Hotazel Formation itself comprises a ~100 m thick package of Fe- and Mn-rich facies that record in their mineral assemblages a complex history. Outcrops of the Hotazel Formation in the Griqualand West Basin feature several Mn- and Fe-rich facies (Fig. 1b) characterized in some outcrops by low-grade, minimally-metamorphosed 'Mamatwan-type' deposits (Gutzmer and Beukes, 1996) that are the focus of this study. Fe-rich lithologies, as classified by James, 1954 and arranged in order of increasing oxidation state of Fe minerals, include silicate-, oxide-carbonate, and oxide-facies iron formation as well as thin, microcystalline beds rich in hematite (Fig. 1b, Tsikos and Moore, 1997; Schneiderhan et al., 2006). Fe-rich lithologies are symmetrically stacked around three Mn-rich sedimentary units: hematite beds sit directly above and below Mn-rich units consisting of braunite, kutnohorite, and hematite, and above and below these hematite beds lie silicate-faces IF containing greenalite [$Fe_6^{2+}Si_4O_{10}(OH)_8$] (Schneiderhan et al., 2006). Previous work has interpreted this symmetric stacking pattern of facies to reflect differences in seawater redox potential, with Mn-rich facies representing precipitation from a stratified water column with higher redox potential than that responsible for the emplacement of Fe-rich facies (Schneiderhan et al., 2006).

As the world's largest deposits of Mn-rich sedimentary rock, hosting approximately 13500 Mt of Mn ore containing >20% Mn (Beukes, 1983; Gutzmer and Beukes, 1996), the Mn-rich facies of the Hotazel Formation are unique within the formation for the wealth of their Mn minerals. Petrographic analysis of the Mn-rich units documented a matrix of microcrystalline braunite and hematite intergrown with kutnohorite hosting abundant ~1 mm carbonate nodules (Tsikos and Moore, 1997; Schneiderhan et al., 2006; Johnson et al., 2016b). Kutnohorite crystals in the matrix are compositionally-zoned and are cross-cut by euhedral braunite (Schneiderhan et al., 2006; Johnson et al., 2016b). Carbonate nodules, consisting mostly of microsparitic kutnohorite, cross-cut the kutnohorite-braunite matrix and rarely contain small inclusions of Mn(IV) oxides interpreted to represent unreacted residues of the primary Mn oxides (Johnson et al., 2016b). While the textures and light $\delta^{13}C$ values preserved in these deposits reflect extensive early diagenetic processing, no organic carbon remains in the Hotazel Formation today, indicating full remineralization of co-deposited organic carbon. The presence of abundant Fe in Mn-rich (28-52 wt. % Mn) units of the Hotazel, constituting 5-24 wt. % Fe of these deposits (Schneiderhan et al., 2006), further suggests the importance of anaerobic Fe cycling in the petrogenesis of these deposits. These petrographic observations imply that the stabilization of Mn(III) phases in the Mn-rich sediments of the Hotazel Formation occurred contemporaneously to complex cycling of Mn and Fe during early diagenesis. Reactions central to Mn and Fe cycling in this deposit, such as anaerobic Fe oxidation by Mn oxides and $Mn^{2+} – Mn^{4+}$ comproportionation, can compete for reactants, requiring consideration of reaction kinetics to predict the initial conditions of organic carbon, Fe oxides and Mn oxides that stabilize Mn(III) precipitates. To address this, we constructed a numerical model describing the kinetics of the involved reactions, calibrated by experimental measurements of the rate constants of these reactions. We then compared our model results to petrographic study of Mn-rich sediments of the Hotazel Formation to evaluate the precise fluxes of organic carbon and Mn-Fe-oxides necessary to stabilize the observed mineral assemblage, providing deeper insight into these ancient and enigmatic rocks.

METHODS

Petrography

A fresh hand sample of Mamatwan-type deposits of the stratigraphically-lowest Mn-rich sedimentary unit of the Hotazel Formation was collected from an open-pit mine in the Kalahari Mn field selected due to its recent exposure and thus lack of oxidative weathering (Johnson et al., 2013, 2016b). A circular ~15 µm ultra-flat thin section was prepared by High Mesa Petrographics and examined using transmitted visible light microscopy as well as spectroscopic X-ray mapping to characterize the mineralogy and petrographic textures of the sample. Prior to this study, this sample had been examined for Mn mineralogy and geochemistry (Johnson et al., 2016b). Transmitted visible light microscopy was performed using a Leica polarizing microscope. For chemical imaging of the Hotazel Formation, we used synchrotron-based X-ray mapping spectroscopic mapping at beamline 10-2 of the Stanford Synchrotron Lightsource in Menlo Park, CA. Maps were created by collecting the X-ray fluorescence generated by incident X-ray light on the thin section, with fluorescence collected by a Vortex SII International Si drift detector for 80 × 80 µm pixels rastered across the thin section. An X-ray energy of 13.5 keV was rastered across the thin section for measurement of elemental abundances. After data collection, each pixel contained information about the energies of fluorescence produced from incident 13.5 keV X-rays proportional to the presence of a given element, allowing for the spatial resolution of different element abundances (Johnson et al., 2016b). The fluorescence maps produced were processed using the MicroAnalysis Toolkit software (Webb, 2006) to produce maps of elemental abundance in mol/cm^3. An

HDF5 file from this processed image was produced and analyzed in Python to calculate Mn^{3+}/Mn^{2+}. This calculation assumed these Mn-rich sediments of the Hotazel Formation are primarily composed of two Mn-bearing phases, kutnohorite and braunite, consistent with previous reports (Johnson et al., 2016b).

Scanning electron microscopy (SEM) and energy-dispersive spectroscopy (SEM-EDS) were used to corroborate and provide additional textural and mineralogical context synchrotron X-ray mapping mapping, and were conducted at Caltech using a Zeiss 1550VP Field Emission SEM equipped with an Oxford INCA Energy 300 X-ray EDS system. Samples were carbon-coated prior to analysis.

Modeling

A numerical model of ordinary differential equations was constructed and solved in MATLAB describing the processes relevant for early diagenesis of Mn-rich sediments. The model tabulated the rate of change of 9 species (MnO_2, MnOOH, $MnCO_3$, Mn^{2+}, FeOOH, $FeCO_3$, Fe^{2+}, lactate, and acetate) and three parameters of the carbonate system:

$$\text{Alkalinity} = [HCO_3^-] + 2[CO_3^{2-}] \qquad (7)$$

$$\text{DIC} = [H_2CO_3] + [HCO_3^-] + [CO_3^{2-}] \qquad (8)$$

$$\text{pH} = -\log[H^+] \qquad (9)$$

The full system of equations is presented in Supplemental Information, but below we describe the rate expressions for components of early diagenesis to facilitate discussion of the results.

The first of the processes relevant for early diagenesis of Mn-rich sediments is microbially-catalyzed remineralization of organic carbon (Eqs. 1, 2). An expression from the literature (Tang et al., 2007) describing the rate of anaerobic oxidation of lactate to acetate and CO_2 by model Mn-reducing bacterium *S. oneindensis* (Myers and Nealson, 1988; Lovley, 1991; Johnson et al., 2016a) was used to represent remineralization of organic carbon by metal-reducing microbes in Mn-rich sediments generally:

$$\frac{d}{dt} = k_3 \cdot \min\left(\left[\mathrm{lac}^-\right], [Metal\ oxide]\right) \frac{k_4}{k_4 + [\mathrm{ace}^-]} \qquad (10)$$

k_3 is an empirically-derived rate constant relating the product of the limiting electron donor or acceptor and a term describing rate attenuation due to accumulation of the metabolic end-product of the metabolism, acetate. For each species interacting with microbial metal reduction (Mn/Fe-oxide, Mn^{2+}/Fe^{2+}), electron flow to a given electron acceptor (MnO_2, FeOOH, or MnOOH) was modeled as proportional to its concentration. The use of a rate expression derived for *S. oneidensis* to represent generalized rates of microbial metal reduction is predicated upon the observation that the extracellular electron transport (EET) logic employed by different metal-oxide-reducing microbes appears to be the product of convergent evolution, despite the fact that sequences encoding metal-reducing biomachinery in extant taxa are highly divergent (cf. (Butler et al., 2009; Richardson et al., 2012)). Critically for the analysis of mixed Fe-Mn formations, however, many these organisms are capable of reducing both Fe and Mn oxides with relatively similar affinity (Lovley, 1991), implying that the physiologies contained within the Fe/Mn-oxide reducing metabolic guild are governed by common chemical logic, even if the biochemical pathways to metal reduction are divergent. In *S. oneidensis*, this moderate indifference to metal-oxide terminal electron acceptor has been demonstrated through studies of metal reduction in a wide range of Fe- and/or Mn-bearing minerals (Lovley, 1991), providing support as well for the acceptor-proportional electron-flow assumption.

The second early diagenetic process contained in the model is the precipitation of carbonates—idealized as two endmembers infrequently observed in Hotazel Formation Mn-rich sediments: siderite and rhodochrosite. Although the Hotazel Formation features prominent kutnohorite rather than rhodochrosite, empirical rate constants for the latter, as well as siderite, were extracted from the literature (Jensen et al., 2002) given the availability of the data. Additionally, the experimental method used by Jensen and coworkers accounts for the kinetic inhibition by Fe^{2+} and Mn^{2+} on Ca-carbonate precipitation hypothesized to be important for Archean carbonates (Sumner and Grotzinger, 1996). Data from Jensen and coworkers were fitted to the common empirical relation (Morel and Hering, 1993), assuming a linear relationship between precipitation rate and the degree of saturation:

$$\frac{d}{dt} = k_{5,6}\left(\frac{[\mathrm{Mn^{2+}},\mathrm{Fe^{2+}}]\left[\mathrm{CO_3^{2-}}\right]}{k_{sp_{rd,sd}}} - 1\right) \qquad (11)$$

The literature contains a range of k_{sp} values for Fe- and Mn-carbonates (Sternbeck, 1997; Jensen et al., 2002; Xu et al., 2004; Bénézeth et al., 2009) due to complexities of carbonate precipitation (Mucci, 2004), but for consistency the k_{sp} values for rhodochrosite and siderite calculated by (Jensen, Boddum, Tjell and Christensen, 2002) were used in this model. The concentration of carbonate ion in the model was calculated for every time step using a modified version of a script solving the carbonate system given dynamic alkalinity and DIC (Zeebe and Wolf-Gladrow, 2001):

$$K_1^{'} = \frac{[\mathrm{HCO_3^-}][\mathrm{H^+}]}{[\mathrm{H_2CO_3}]} \qquad (12)$$

$$K_2^{'} = \frac{[\mathrm{CO_3^{2-}}][\mathrm{H^+}]}{[\mathrm{HCO_3^-}]} \qquad (13)$$

Together with Eqs. 6 and 7, Eqs. 11 and 12 formed a system of 4 equations and 4 unknowns that could be readily solved given DIC and alkalinity from the model and values for $K_1^{'}$ *and* $K_2^{'}$ from the literature. Initial values of 2300 and 2000 meq were assigned for alkalinity and DIC, respectively, selected due to the plausibility that Precambrian seawater had carbonate chemistry broadly similar to that of the modern (Grotzinger and Kasting, 1993; Grotzinger and James, 2000; Hardie, 2003; Sumner and Beukes, 2006; Higgins et al., 2009; Spear et al., 2014; Halevy and Bachan, 2017).

Reduction of MnO_2 by $Fe^{2+}_{(aq)}$ was studied in the model; this process was inferred to be important in Mn-rich sediments given the co-occurence of hematite with kutnohorite throughout the Hotazel Formation and in close (μm-scale) petrographic association (Schneiderhan, Gutzmer, Strauss, Mezger and Beukes, 2006). This reaction is known to be rapid (Villinski, Saiers and Conklin, 2003; Siebecker, Madison and Luther, 2015; Johnson, Savalia, Davis, Kocar, Webb, Nealson and Fischer, 2016) but self-limiting, due to the accumulation of Fe-oxides such as lepidocrocite, which occludes reactive sites on the MnO_2 surface, preventing further reaction with dissolved Fe^{2+}. The reaction between Fe^{2+} and MnO_2 is modeled here (after (Villinski, Saiers and Conklin, 2003)) as second-order with respect to the two reactants:

$$\frac{d}{dt} = k_1[\mathrm{MnO_2}][\mathrm{Fe^{2+}}] \qquad (14)$$

The final modeled component of the early diagenesis system was the comproportionation reaction between Mn^{2+} and MnO_2 to produce Mn(III) phases (Eq. 4). Work on the kinetics of this reaction has documented the complexity of the reaction pathways involved (Lefkowitz, Rouff and Elzinga, 2013), but the equilibrium stability of these phases can be generally described by the relation:

$$K_{eq} = \frac{[\mathrm{H^+}]^2}{[\mathrm{Mn^{2+}}]} \qquad (15)$$

For the comproportionation reaction to proceed, the thermodynamic threshold described above must be exceeded, i.e. $[Mn^{2+}] > [H^+]^2 / K_{eq}$. Although the nanoparticulate nature of initial Mn^{3+} precipitates creates significant uncertainties in estimates of these thresholds (Navrotsky et al., 2010; Lefkowitz et al., 2013), for the purposes of modeling here, a K_{eq} for feitknechtite of $10^{-10.2}$ calculated by Lefkowitz and coworkers was used, given experimental observations of feitknechtite as a primary precipitate of the Mn^{2+}–MnO_2 comproportionation reaction. Data from a kinetic experiment conducted by

Lefkowitz and coworkers that produced hausmannite (no data was available for feitknechtite) was fitted assuming a first-order reaction with respect to [Mn^{2+}]:

$$\frac{d}{dt} = k_2[\mathrm{Mn}^{2+}] \qquad (16)$$

The four component rate relations outlined above were assembled into a system of 9 ordinary differential equations according to the network topology of early diagenetic chemical reactions diagrammed in Fig. 2. With initial organic carbon (represented in the model by lactate) set to 1 mM, initial FeOOH and MnO_2 concentrations were each varied between 0.01–15 mM, and the system of differential equations was solved using the Runge-Kutta method of MATLAB's *ode45* solver (Shampine and Reichelt, 1997), producing a 75x75x11 matrix with entries representing the steady-state concentrations of each of the 9 species, alkalinity and DIC. At every timestep, pH was calculated from carbonate alkalinity and DIC using the equations of Zeebe and Wolf-Gladrow. The dimensions of the matrix were set by the length of the respective vectors describing independent variables of initial [FeOOH], [MnO_2], and [lactate].

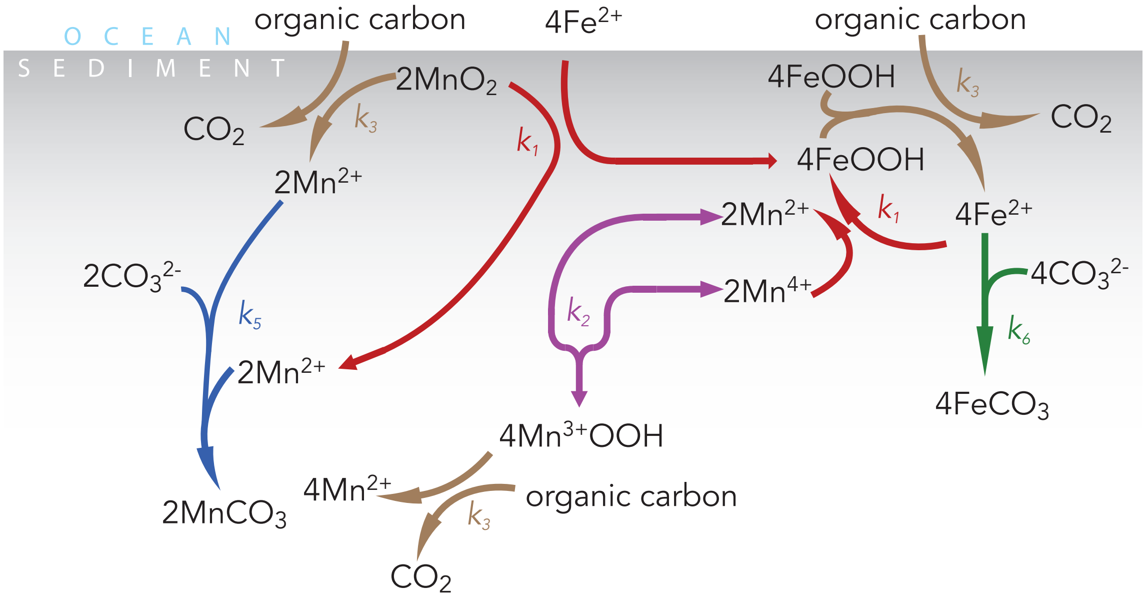

Figure 2. Schematic representation of chemical reactions in the early diagenesis of Mn-rich sediments modeled in this study. Corresponding rate constants were placed in Table 1.

Constant	Value	Citation
k_1	5500	Villinski, et al. 2003
k_2	140	Elzinga, et al. 2011
k_3	0.33	Tang, et al. 2007
k_4	0.0126	Tang, et al. 2007
k_5	7×10^{-11}	Jensen, et al. 2002
k_6	1×10^{-8}	Jensen, et al. 2002
k_7	2×10^{-6}	Jensen, et al. 2002
k_{sprd}	6.3×10^{-13}	Jensen, et al. 2002
k_{spsd}	1.4×10^{-11}	Jensen, et al. 2002
k_{spcc}	$1 \times 10^{-8.5}$	Jensen, et al. 2002

Table 1. Values for rate constants and other parameters used in the numerical model of the early diagenesis of Mn-rich sediment. Rate constant indices correspond to those depicted in Figure 1.

RESULTS

Microscopy

Optical microscopy, synchrotron X-ray mapping, and SEM-EDS analysis of a thin section sample of the Hotazel Formation corroborated earlier reports characterizing this facies of the formation as dominated by mixed Fe and Mn phases and mm-scale carbonate nodules (Fig. 3). Optical microscopy indicated the presence of pervasive nodules with diffuse margins throughout these Mn-rich sediments. Nodule centers contained drusy crystals with larger crystal sizes near their centers, decreasing in size toward more finely crystalline and nodule margins (Fig. 3A).

SEM imaging exhibited several intergrown phases within the nodules and matrix distinguished by the intensity of the backscatter and their elemental composition inferred from SEM-EDS (Fig. 3b). 100 µm-scale textures are characterized by phases with higher (located in the matrix) or lower (localized in nodules) backscatter signatures. Rare euhedral high-backscatter phases were observed in nodules, high-backscatter phases were predominantly found in the matrix. Minerals appearing darkest under SEM backscatter were typically cross-cut by euhedral crystals of a brighter (higher-backscatter) phase, which were in turn cross-cut by yet brighter phases. SEM-EDS mapping indicates these three phases correspond to minerals rich in Ca+Mn, Mn+Si, and Fe+O, respectively (Fig. 3b). These mineralogical and textural observations are consistent with descriptions in the literature (Schneiderhan et al., 2006; Johnson et al., 2016b) of kutnohorite, braunite, and hematite in this unit of the Hotazel Formation.

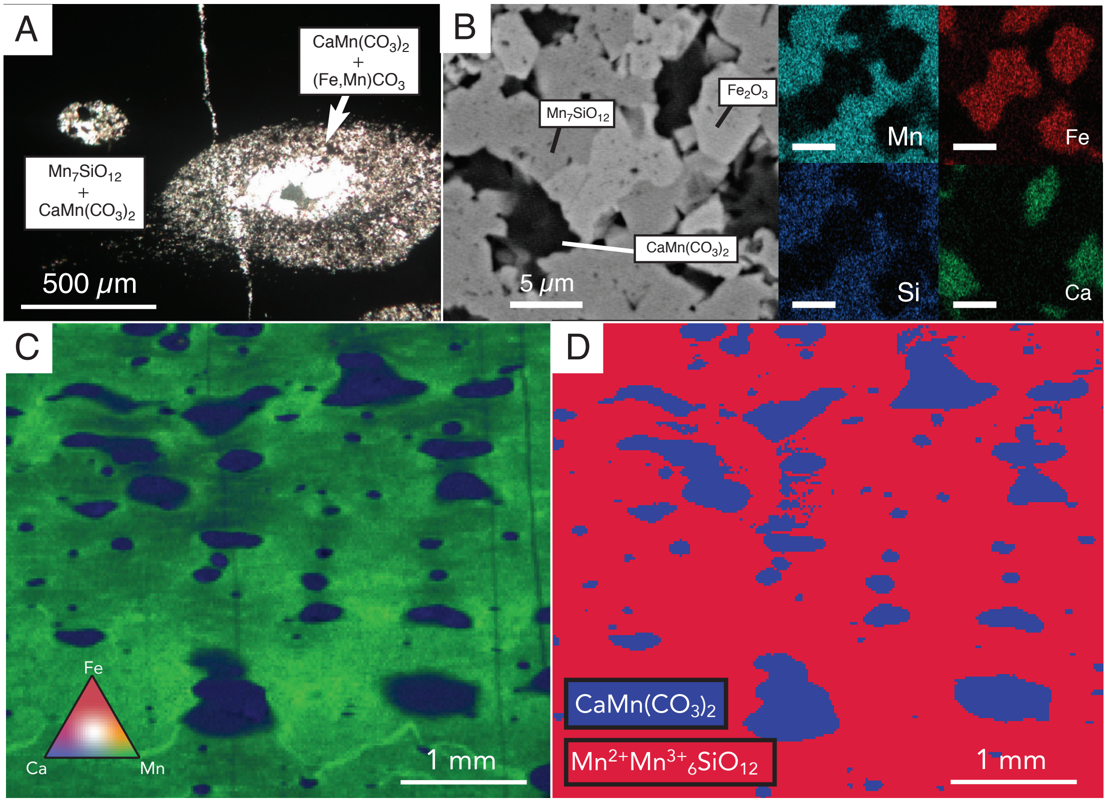

Figure 3.—SEM-EDS microscopy and synchrotron XRF and XAS analyses of a thin section of Mn-rich sedimentary rock from the Hotazel Formation. **A**) Transmitted-light optical microscopy. **B**) SEM (left panel) and EDS (right) showing intergrown braunite, hematite, and kutnohorite in Mn-rich sediments of the Hotazel Formation. **C**) Synchrotron XRF mapping at a beam energy of 13.5 keV, showing fluorescence detected from Mn, Fe, and Ca. **D**) Segmented image of Mn fluorescence from synchrotron XRF mapping, showing distribution of kutnohorite (blue) and braunite (red). See text for details. Figure 4.—Steady-state mineral assemblages calculated by the numerical model of early diagenesis of Mn-rich sediments with initial C_{org} = 1 mM. Notable initial conditions (A-C) were highlighted.

Larger-scale textural relationships were revealed and quantified through synchrotron-based X-ray microprobe spectroscopy mapping. High-energy X-ray mapping at 13500 eV documented the relative spatial distribution of Fe, Mn, and Ca in the sample (Fig. 3C). Fe and Mn were found at higher concentrations in the matrix (up to 2.3 and 9.5 mol/cm^2, respectively) and Ca was found at higher concentrations in nodules (Fig. 3C). Elevated Fe relative to Mn was detected around nodule margins, appearing on 3-color maps of Fe, Mn and Ca concentrations as lighter green areas, with darkest green describing areas richest in Mn. Mapping of relative Fe, Mn, and Ca revealed the abundance of Mn relative to these other two important cations throughout the sample, corroborating earlier geochemical reports characterizing elemental abundances in hand samples of this unit of the Hotazel via bulk rock XRF methods (Schneiderhan et al., 2006). This previous work described bulk Mn, Fe, and Ca abundances from this unit ranging from 5.1-24.1%, 28.2-51.6%, and 6.1-22.9% by weight, respectively; on average, Mn, Fe, and Ca abundances average 10.2%, 40.7%, and 17%, respectively (Schneiderhan et al., 2006). These data, reflecting bulk Mn/Fe ≈ 4 averaged over 12 hand samples from the lowest Mn-sediment unit of the Hotazel, strongly agree with our measurement of Mn/Fe ≈ 4.4 averaged over the thin section collected from this unit, reinforcing our confidence in the quantitative capabilities of our synchrotron-based methods.

After characterizing the spatial distribution and relative abundance of Fe, Mn, and Ca in the sample, we quantified the distribution of Mn redox states in this sample of Mn-rich sediments of the Hotazel Formation, leveraging previous observations that matrix-hosted Mn is contained in braunite ($Mn^{3+}/Mn^{2+} = 6$), while nodules contain Mn in kutnohorite ($Mn^{3+}/Mn^{2+} = 0$) (Schneiderhan et al., 2006; Johnson et al., 2016b). Pixels representing Mn fluorescence from nodules, and therefore from kutnohorite-bound Mn, appeared as a distinct population of pixels with lower fluorescence from Mn, and thus lower Mn concentration. This bimodal distribution of Mn fluorescence intensities was used to segment the image using a threshold intensity value, yielding two pixel populations (Fig. 3D). Two sums of the pixel intensities in these two populations was weighted by Mn^{2+} and Mn^{3+} content of each phase, and the ratio of these sums yielded $Mn^{3+}/Mn^{2+} = 4.2$.

Numerical Modeling

The presence of co-occurring ferrous Fe species with Mn oxides defines a disequilibrium mineral assemblage that combats simple thermodynamic treatment, and therefore a model was constructed that could evaluate the kinetics required to explain this complex deposit. This model varied initial [FeOOH], [MnO_2], and [lactate]. The last parameter is a stand-in that represents reactive organic carbon, selected due to the abundance of kinetic data on lactate oxidation by metal-oxide reducing microbes (Tang et al., 2007). The model produced steady state values of [$MnCO_3$], [$FeCO_3$], [FeOOH], [$Mn^{3+}OOH$], and [MnO_2], creating mineral assemblages *in silico* that could be compared to the observed assemblage in the Hotazel Formation. (Figs. 4-6). Initial [FeOOH] and [MnO_2] values were varied between 0.01-15 mM and initial [lactate] was set to 1 mM. The range of final mineral stable mineral assemblages were visualized using contour plots that depicted the dominant mineral phases (i.e. $MnCO_3$, $FeCO_3$, FeOOH, $Mn^{3+}OOH$, and MnO_2) for a given initial [lactate] across a 2D space defined by a range of initial [FeOOH] and [MnO_2].

Modeling results depicted two broad behavior domains of the system, producing a final mineral assemblage dominated by $MnCO_3$ and $FeCO_3$ and one dominated by FeOOH, MnOOH, and MnO_2, divided by a line with slope corresponding to the stoichiometry of MnO_2 and FeOOH reduction via 4 e^- transfer by oxidation of lactate to acetate (Fig. 4). The relative concentrations of $MnCO_3$ and $FeCO_3$ in the domain corresponding to a $MnCO_3$ – $FeCO_3$ mixture reflected amounts that were directly proportional to initial [MnO_2]/[FeOOH]. The proportionality of these final carbonate phases to the relative amount of initial oxide phases was apparent from the slope of the contours of each respective phase, radiating outwards from the origin (Fig. 4). The domain corresponding to a final mineral assemblage dominated by FeOOH, MnOOH, and MnO_2 was broadly characterized by a maximum final MnOOH content representing balance between relative C_{org} and MnO_2 supply. A set of initial conditions with relatively low initial FeOOH and higher MnO_2 produced abundant final MnOOH, the relative lack of Fe allowing for higher % Mn phases, but insufficient initial MnO_2 to result in mineral assemblages without sufficient electron donors to reduce a significant amount of MnO_2.

Estimates of initial conditions corresponding to the observed steady-state mineral assemblage in the Hotazel Formation were made by contouring [Mn]/[Fe] and MnOOH/$MnCO_3$ ratios–measured using synchrotron X-ray mapping–in initial [MnO_2] – [FeOOH] space as calculated by the numerical model. Values for these contours—

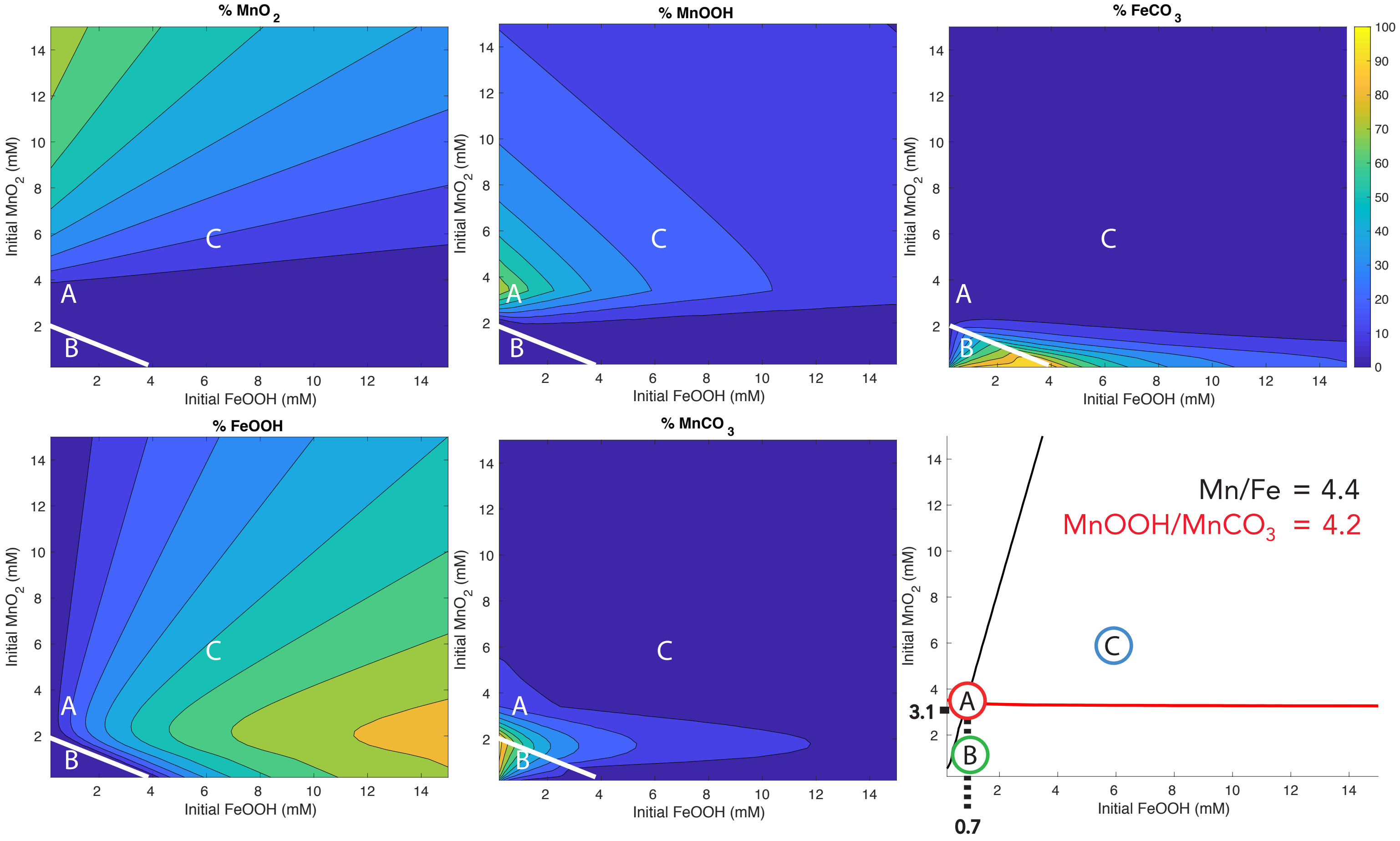

Figure 4.—Steady-state mineral assemblages calculated by the numerical model of early diagenesis of Mn-rich sediments with initial C_{org} = 1 mM. Notable initial conditions (A-C) were highlighted.

describing the set of solutions for mapping a range of initial [MnO_2], [FeOOH], and [lactate] to a [Mn]/[Fe] or $FeCO_3$ per total Fe—were determined from quantification of synchrotron observations of a sample of the Hotazel Formation, giving values of [Mn]/[Fe] ≈ 4.4 and MnOOH/$MnCO_3$ ≈ 4.2 (Fig. 4). Intersection of the contours indicated that the initial conditions capable of reproducing the observed mineral assemblage in the Hotazel Formation was only possible for initial [FeOOH] : [MnO_2] : [lactate] ≈ 0.7 : 3.1 : 1 (Fig. 4, point A). The contour describing [Mn]/[Fe] traced out a line from the origin with an approximate slope of ~4, reflecting the absence of removal of dissolved Mn^{2+} or Fe^{2+} via advective or diffusive transport processes in this model. The contour describing solutions corresponding to Fe_2O_3 per total solid phase Fe displayed a sharp kink at higher initial [FeOOH] that resulted from the decreasing degree of FeOOH reduction with higher initial [FeOOH], resulting in increasing residual FeOOH and decreasing final $FeCO_3$.

Two other points of interest (points B and C) were also selected, representative of initial [Mn]/[Fe] = 1 in domains corresponding to $MnCO_3$+$FeCO_3$- and FeOOH+MnO_2+MnOOH-dominated mixtures. A ternary plot summarizing solutions to the model for initial [lactate] = 1 mM was also constructed (Fig. 5). The model proved incapable of producing solutions containing MnO_2 residues for $MnCO_3$: MnOOH lower than ~1:4. The model, however, was able to produce $MnCO_3$-rich solutions in cases where no MnO_2 residues remained. An overlay of % $FeCO_3$ per total Fe onto these data revealed correlation between the relative abundance of reduced Fe species and that of reduced Mn (Fig. 5).

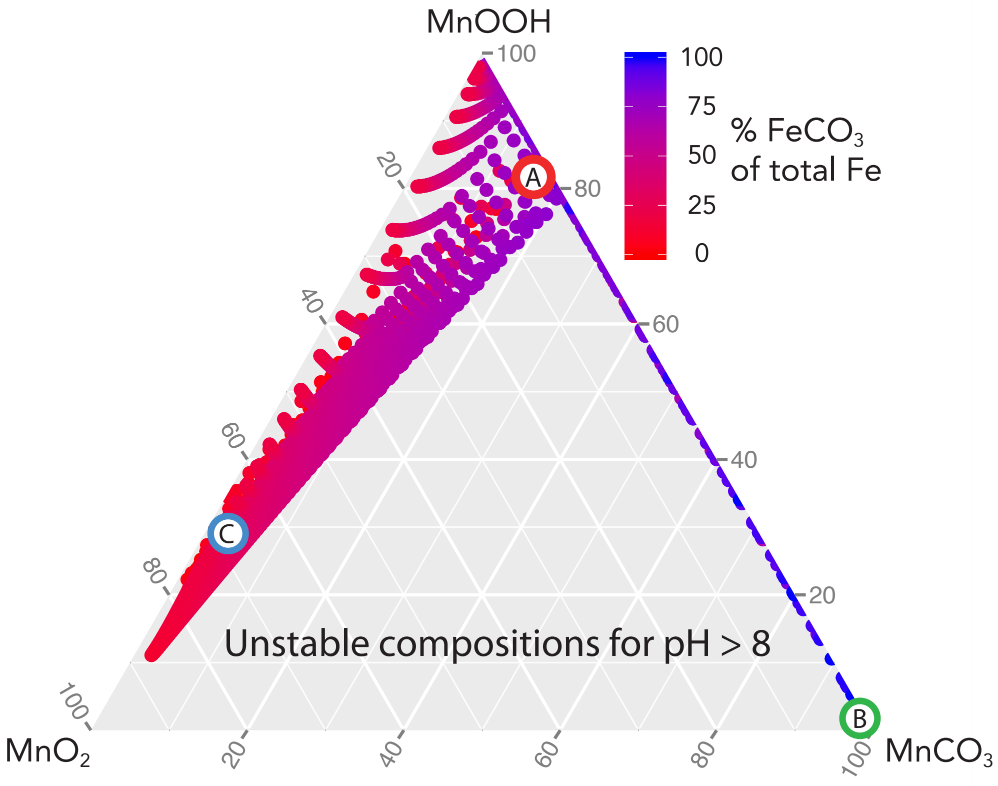

Figure 5.—Ternary plot summarizing steady-state mineral assemblages calculated by the numerical model of early diagenesis of Mn-rich sediments with initial C_{org} = 1 mM. Notable initial conditions (A-C) were highlighted as detailed in the text and in Fig. 4.

The time-dependent behavior of this system, for three selected representative initial conditions corresponding to points A, B, and C in initial [MnO_2] – [FeOOH] space (cf. Fig. 4), exhibited a clear bifurcation in the products generated by this system (Fig. 6). For initial condition A, % MnOOH increased logistically and simultaneously with % $FeCO_3$ and % $MnCO_3$ while % MnO_2 and % FeOOH decreased symmetrically with % MnOOH and % $FeCO_3$. Initial condition B, corresponding to [Mn]/[Fe] = 1 within the set of $MnCO_3$+$FeCO_3$-dominated solutions, displayed complex behavior in which % MnOOH increased until % MnO_2 reaches zero, after which % MnOOH decreased to zero. Subsequently, % $MnCO_3$ increased while $FeCO_3$ fell significantly. Initial condition C depicted small logistic increases in % $FeCO_3$, % MnOOH, and % $MnCO_3$ at the expense of % FeOOH and % MnO_2 (Tang et al., 2007).

Varying the rate constant describing metal oxide reduction via lactate (representative of sedimentary organic carbon) oxidation (k_3) across 8 orders of magnitude while initial FeOOH : MnO_2 : C_{org} was held constant at 0.7 : 3.1 : 1 revealed a bifurcation of steady-state solutions to the early diagenesis system with respect to solid phase Mn species, i.e. MnO_2, MnOOH, and $MnCO_3$ (Fig. 7). For k_3 values >5 orders of magnitude slower than initially modeled (cf. Figs. 4-6), MnOOH as a percentage of total solid phase Mn decreased to near zero, replaced instead by an MnO_2+$MnCO_3$ mixture. Decreases in MnOOH and $MnCO_3$ as a proportion of solid phase Mn were accompanied by MnO_2 increases in steady-state solutions corresponding to small ($<10^{-6}$) k_3.

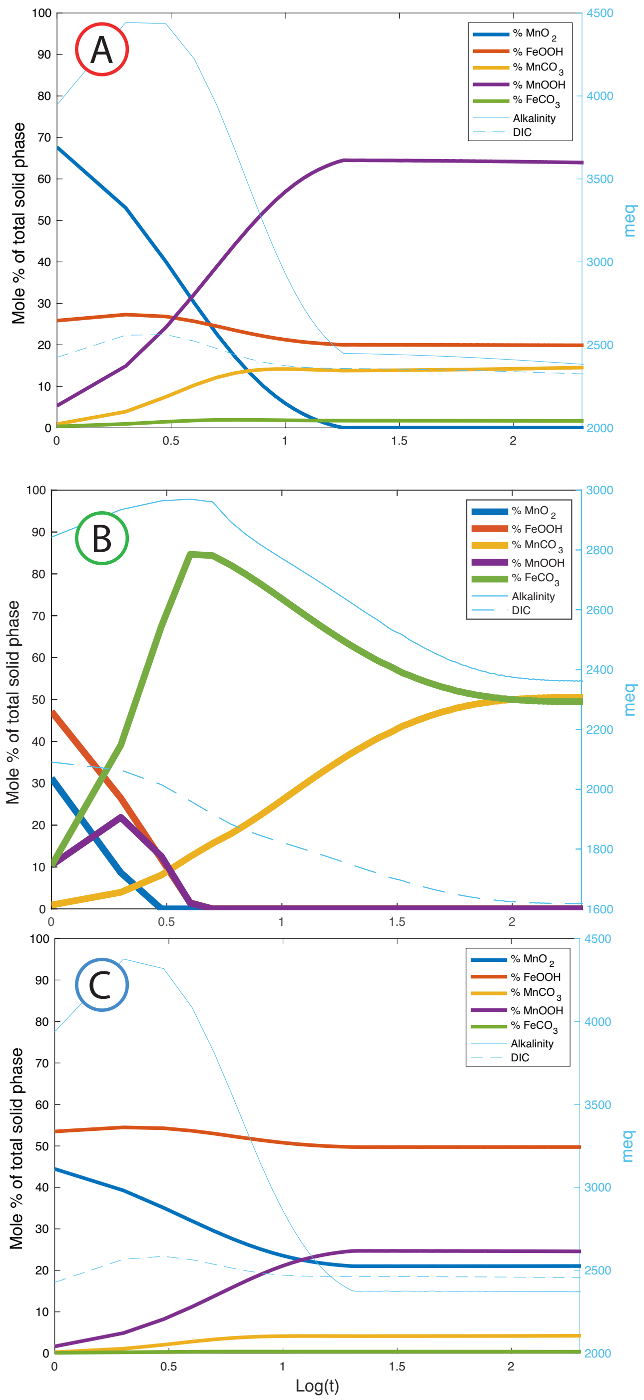

Figure 6.—Time-dependent behavior of three runs of the numerical model corresponding to initial conditions A-C annotated in Figs. 4, 5.

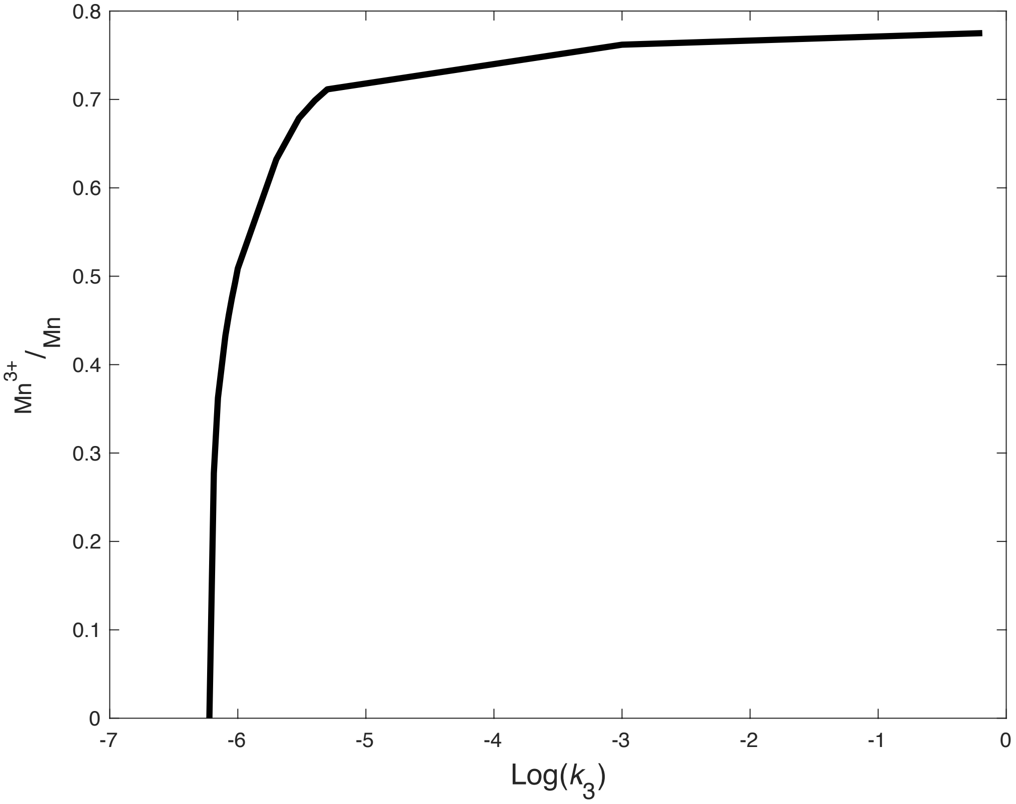

Figure 7.—Dependency of final $MnOOH/MnCO_3$ ratio of mineral assemblage on rate constant for microbial metal reduction (k_3). For $k_3 < \sim 6 \times 10^{-6}$, MnOOH cannot be precipitated by the early diagenetic system as modeled here (dashed line).

DISCUSSION

Petrographic characterization of this sample of the Hotazel Formation by SEM-EDS and synchrotron-based XRF mapping revealed a complex early diagenetic history recorded by this deposit. SEM-EDS documented braunite, kutnohorite, and hematite phases dispersed in a matrix and cross-cut by carbonate nodules containing kutnohorite (Fig. 3). Kutnohorite-bearing carbonate nodules were in turn cross-cut by later braunite and hematite phases, reflecting a diagenetic history with multiple stages of carbonate and silicate/oxide precipitation. These observations corroborate previous work identifying chemical zoning in kutnohorite of the Hotazel Formation, interpreted as representative of dynamic early diagenetic processes responsible for the precipitation of kutnohorites with variable cation concentrations (Johnson, Webb, Ma and Fischer, 2016). Our quantification of Mn^{3+}/Mn^{2+} (≈ 4.2) in the Hotazel Formation corroborated previous reports of the abundance of the Mn^{3+}-rich phase braunite, interpreted to represent an earlier $Mn^{3+}OOH$ phase which subsequently reacted with porewater Si to form braunite (Johnson et al., 2016b).

The presence of a Mn^{3+} phase thought to be stabilized by reactions between $Mn^{4+}O_2$ phases and $Mn^{2+}_{(aq)}$ (Lefkowitz et al., 2013), required the evaluation of the kinetics of reactions relevant for Mn and Fe phases constituting the primary Mn-rich sediments, which would allow for time-varying and disequilibrium processes that we postulated might stabilize the observed mineral assemblage. These kinetics were evaluated by a numerical model describing processes relevant for early diagenesis of Mn-rich sediments, and produced stable mineral assemblages grouped into $MnCO_3$+$FeCO_3$ -

rich and MnOOH+MnO_2+FeOOH-rich assemblages, divided by a line with slope corresponding to the stoichiometric oxidation of lactate (used in the model as a substitute for organic carbon) coupled to the reduction of MnO_2 or FeOOH, and mediated by a metal-reducing microbe (e.g. *S. oneidensis*). Varying initial [lactate] translated this stoichiometric line outwards from the origin without changing slope (data not shown), demonstrating the insensitivity of this modeling approach to differing absolute concentrations; although the concentrations modeled here (with maxima = 15 mM) are clearly lower than those in a package of primary Mn- and Fe-oxide sediments, changes in absolute concentrations do not change the behavior of the system. Instead, these results showed that insight into the early diagenetic dynamics of mixed Fe- and Mn-oxide sediments using this modeling approach could be obtained by varying the relative concentrations of three inputs: FeOOH, MnO_2, and lactate.

Solutions to the $MnCO_3$+$FeCO_3$ -rich and MnOOH+MnO_2+FeOOH-rich domains correspond to those with electron-acceptor-limiting and electron-donor-limiting initial conditions, respectively (Fig. 4). Within the electron-acceptor-limiting domain, solutions describe a mixture of Mn and Fe carbonates with $MnCO_3$: $FeCO_3$ varying in direct proportion to initial MnO_2 : FeOOH. Thus, this domain retains no information to constrain the proportion of initial organic carbon required to produce the deposit, as the final composition of the mineral assemblage is entirely dependent on initial FeOOH and MnO_2. Contours for carbonate phases above the electron-donor-limiting frontier change slope from contours within the electron-acceptor-limiting initial conditions set, reflecting the presence of partially- or non-reduced oxide phases above this stoichiometric line. The set of solutions dominated by MnOOH (up to 92.5%) are of particular note, as these contain solutions analogous to that of the Hotazel Formation, consisting of significant Mn^{3+} species proposed (Johnson, Webb, Ma and Fischer, 2016) to have formed from comproportionation of Mn^{2+} and Mn^{4+} through an analogous mechanism to that modeled here using experimental constraints (Elzinga, 2011; Lefkowitz, Rouff and Elzinga, 2013; Johnson, Savalia, Davis, Kocar, Webb, Nealson and Fischer, 2016). Indeed, it is in this region that the contours–describing the set of solutions corresponding to ratios constrained by synchrotron XRF–intersected, indicating initial relative concentrations of FeOOH, MnO_2, and organic carbon were likely near 0.7 : 3.1 : 1 (Figs. 4-6, point A). Additionally, for large (>6 times the initial concentration of electron-donor) initial electron acceptor concentrations, the behavior of the system resembles that of the set of electron-acceptor-limiting solutions, reflecting insufficient electron donor concentrations to produce final $MnCO_3$: $FeCO_3$ ratios that differ from initial MnO_2 : $FeCO_3$.

Visualizing solutions for this system with initial [lactate] = 1 mM in ternary space illustrated important aspects of the general behavior of Mn-rich sediments undergoing microbially-catalyzed early diagenesis (Fig. 5). Stable mineral assemblages fell within a field on the ternary diagram clearly demarcated by a line from the 100% MnO_2 corner describing a constant ratio of 1:4 $MnCO_3$: MnOOH that the set of solutions with remaining unreduced MnO_2 residue cannot exceed. This is a direct result of the importance of the Mn^{2+}-Mn^{4+} comproportionation reaction in the early diagenesis of Mn-rich sediments, which for porewater pH ≥ 8 (reflecting syn-depositional conditions for the Hotazel Formation) is favorable as long as $Mn^{2+}_{(aq)}$ and MnO_2 are both in excess of

~100 μM (Lefkowitz et al., 2013). Relatively acidic porewater ($pH < 8$) were required to drive MnOOH disproportionation, producing mineral assemblages dominated by co-existing $MnCO_3$ and MnO_2. Thus, for likely syn-depositional pH conditions and sufficient Mn^{2+} and MnO_2, Mn^{2+}-Mn^{4+} comproportionation- was strongly favored, producing Mn mineral assemblages dominated by Mn(III).

The time-dependent behavior of this system was then examined, allowing for direct comparison between the behavior of the model and the history of the retrieved sample of the Hotazel Formation as inferred by investigation of cross-cutting relationships (Fig. 6). For initial [FeOOH], [lactate], and [MnO_2] found to produce in the model a mineral assemblage similar to that of the Hotazel, the time-dependent behavior delineated a history in which early MnOOH precipitation was followed by later precipitation of $MnCO_3$ and $FeCO_3$ (Fig. 6A). This somewhat contradicts textural observations of the Hotazel Formation in which the Mn^{3+} phase both cross-cuts and is cross-cut by kutnohorite, the former as a cement and the latter as nodules. The modeling performed here did not account for localized precipitation of nodules around nuclei, which could ameliorate this problem. Additionally, braunite has been interpreted to result from silica uptake by a MnOOH precursor (Johnson et al., 2016b), suggesting that primary cross-cutting relationships may not have been preserved in the rock record.

The time-dependent behavior of one set of initial conditions corresponding to electron-acceptor limitation (Fig. 6B) further demonstrated the importance of time-resolved understandings of these processes. For conditions corresponding to electron acceptor limitation and initial [MnO_2] : [FeOOH], the model produced a metastable initial mineral assemblage with ~20% MnOOH that subsequently dissolved as MnO_2 is depleted by reductive dissolution. Without MnO_2 to react with $Mn^{2+}_{(aq)}$, MnOOH disproportionated as $MnCO_3$ decreased $[Mn^{2+}_{(aq)}]$ below the K_{eq} for the comproportionation reaction, dissolving the metastable phase. Additionally, a small deviation from the 1:1 $[MnCO_3]$: $[FeCO_3]$ expected for initial 1:1 $[MnO_2]$: [FeOOH] and electron-acceptor-limited conditions was observed, resulting from the fast precipitation of $FeCO_3$ relative to $MnCO_3$. Rapid sequestration of CO_3^{2-} in $FeCO_3$ reduced DIC and resulted in $[Mn^{2+}_{(aq)}]/[Fe^{2+}_{(aq)}] > 1$.

Mn^{4+}–Mn^{2+} comproportionation was observed in these numerical experiments to be crucial for the production of solid-phase Mn(III) in analogous abundance to that observed in the Hotazel Formation. Abundant carbonate anion in marine environments has provided a sink for Mn^{2+} throughout much of Earth history, implying that $[Mn^{2+}_{(aq)}]$ was unlikely to have exceeded the ~100 μM requirement for spontaneous Mn^{4+}–Mn^{2+} comproportionation on the basis of fluxes from the solid earth alone. Production of Mn^{2+} from reductive dissolution of MnO_2, however, might have provided sufficient Mn^{2+} to drive Mn^{4+}–Mn^{2+} comproportionation and thus precipitate abundant MnOOH. Without rapid production of Mn^{2+} from reductive dissolution, $[Mn^{2+}_{(aq)}]$ could not have reached concentrations sufficient for comproportionation with solid-phase Mn(IV). This was demonstrated quantitatively in our model results by a bifurcation of model solutions across a threshold value for the metal reduction rate constant parameter $k_3 \leq 6 \times 10^{-.6}$ (Fig. 7), five orders of magnitude slower than the rate constant determined from experimental studies of *S. oneidensis* (Tang et al., 2007).

Invoking reductive dissolution of MnO_2 as a crucial aspect in the petrogenesis of the Hotazel Formation requires a significant supply of reductant to the precursor sediments. As modeled here, this reductant was likely organic carbon as other titrants (e.g. sulfide) would have resulted in the accumulation of insoluble products not observed in the Hotazel Formation (e.g. elemental sulfur). In contrast, a flux of organic carbon into precursor sediments of the Hotazel Formation would have ultimately produced CO_2 upon complete remineralization, leaving the stable mineral assemblage devoid of organic carbon. Additionally, the possibility that $Fe^{2+}_{(aq)}$ could have served as a reductant is also precluded by our kinetic approach to modeling Hotazel Formation petrogenesis, as the weathering flux of $Fe^{2+}_{(aq)}$ to the ocean would not have provided a sufficient flux of electron equivalents to drive Mn^{4+}–Mn^{2+} comproportionation. Using the numerical experiments presented here as a comparison, estimates of a weathering flux of ~10^{12} mol Fe yr^{-1} (Canfield, 1998; Holland, 2006) would represent a flux of ~10^{-6} – 10^{-9} mmol e^{-} yr^{-1} from $Fe^{2+}_{(aq)}$ into a 1 L volume of seawater depending on the estimated volume of seawater into which the $Fe^{2+}_{(aq)}$ efflux entered and is mixed on an annual timescale. In contrast, the transfer of electrons from 1 mM C_{org} occurred at a rate equivalent to $6x10^{3}$ mmol e^{-} yr^{-1} in our numerical experiments. Reducing the metal reduction rate parameter k_3 to a value insufficient to produce MnOOH by comproportionation ($k_3 \leq 10^{-6}$) was equivalent to an electron transfer rate of 10^{-2} mmol e^{-} yr^{-1}, still several orders of magnitude faster than estimates of electron flux via $Fe^{2+}_{(aq)}$ from weathering, thus precluding $Fe^{2+}_{(aq)}$ from weathering as a potential source of reductant to produce MnOOH precursor phases of braunite in the Hotazel Formation.

It was clear from these results that catalyzed Mn-oxide reduction (usually performed in modern sediments by microbial dissimilatory metal reduction) was necessary to accumulate sufficient Mn^{2+} to drive comproportionation and therefore produce abundant Mn(III) phases. The insight that Mn(III) phases suggest a history of microbially-mediated reductive dissolution of MnO_2 may provide a framework to interpret potential biosignatures in Mn-rich martian rocks (Lanza et al., 2014). If these martian units share a chemical sedimentary petrogenesis with Mn-rich sedimentary rocks of the Hotazel Formation, they may record a history of microbially-catalyzed Mn reduction if the presence of Mn(III) phases were to be discerned.

The inference that a ratio of initial FeOOH : MnO_2 : C_{org} = 0.7 : 3.1 : 1 was required to produce the mineral assemblage observed in the Hotazel Formation enabled further interpretation of the paleoenvironment recorded by the Hotazel Formation. Previous studies have characterized the stacking pattern of iron- and manganese-rich facies of the Hotazel Formation as the result of fluctuating seawater redox conditions, given the necessity for highly oxidizing conditions to oxidize $Mn^{2+}_{(aq)}$ relative to that required for oxidation of $Fe^{2+}_{(aq)}$ (Beukes, 1983; Schneiderhan et al., 2006; Lantink et al., 2018). However, the significant excess of seawater $Mn^{2+}_{(aq)}$ relative to $Fe^{2+}_{(aq)}$ necessary to produce sedimentary metal oxides of a similar ratio required a mechanism by which Mn is enriched in seawater relative to Fe, as Fe from the solid earth is in significant excess relative to Mn (Fe : Mn in upper continental crust ≈ 60 : 1, (Taylor and McLennan, 1995)). Differing oxidation kinetics between $Fe^{2+}_{(aq)}$ and $Mn^{2+}_{(aq)}$ offer an explanation. $Fe^{2+}_{(aq)}$ is readily oxidized relative to Mn^{2+} (Millero et al., 1987; Morgan, 2005; Luther, 2010), resulting in depletion of Fe relative to Mn as a parcel of metal-rich, upwelling seawater reacts with atmospheric O_2. Transport of this water parcel in communication with atmospheric O_2 would result in progressively Mn-dominated metal oxide sediments, resulting finally in the deposits analyzed here, with primary FeOOH : MnO_2 ratios of 1 : 4.4. Changes of facies in the Hotazel Formation from Fe- to Mn-dominated could thus be reinterpreted to result from changing proximity of the Hotazel Formation depocenter with respect to an initial upwelling zone, with Mn-rich facies corresponding to a greater distance to the upwelling zone.

More broadly, the precipitation and stabilization of phases in the numerical model not predicted by thermodynamics demonstrated the importance of kinetic parameters (Elzinga, 2011) in reconstructing paleoenvironments and active pathways which were likely to have processed manganese formations in the deep past. In particular, the stable mineral assemblage represented by point A (analogous to that in the Hotazel Formation), consisting of >50% of a braunite-precursor Mn(III) phase, demonstrates the importance of rapid accumulation of $Mn^{2+}_{(aq)}$ and the subsequent comproportionation reaction with Mn^{4+} in determining the outcome of early diagenesis of these Fe-Mn sediments. The capacity for this numerical model to reproduce the mineral assemblage of the Hotazel Formation indicates the importance of examining reaction kinetics in systems where fluxes may be modulated by biology. Differences in reaction products from a model variant excluding biological Fe and Mn reduction further underscores the importance of evaluating effects of biological modification of manganese formations when examining Fe and Mn formations.

CONCLUSIONS

The Hotazel Formation—though notably devoid of significant concentrations of organic carbon today—records a rich history of active interaction with organic carbon, demonstrated here by the diagenetically stabilized, disequilibrium mineral assemblage constrained through coupled spectroscopic and modeling efforts. Synchrotron X-ray mapping of a Mn-rich facies of the Hotazel Formation with prominent early diagenetic textures (e.g. nodules) revealed the coexistence of Mn and Fe phases out of thermodynamic equilibrium, requiring kinetic explanations. A numerical model of the early diagenesis of Mn-rich sediments was used to invert for initial concentrations of electron donor and electron acceptors (FeOOH and MnO_2) required to produce the mineral assemblage measured by synchrotron X-ray techniques, and indicated that initial $[FeOOH] : [MnO_2] : [C_{org}] = 0.7 : 3.1 : 1$. These ratios reflect an input of significant C_{org} to the precursor sediments that is today absent due to remineralization during early diagenesis. Additionally, the model demonstrated that rapid Mn^{2+} production from reductive dissolution of MnO_2 by C_{org} was necessary to produce final concentrations of solid-phase Mn^{3+} matching that measured in the Hotazel Formation by synchrotron XRF. The kinetically controlled reactions resulting from C_{org} remineralization increased Mn^{2+} concentrations in porewaters fast enough to drive comproportion with Mn^{4+}, ultimately resulting in an abundant Mn^{3+} phase that would later become braunite after diagenetic reactions with porewater Si. These results indicate these Mn deposits are very much geobiological in nature—not just requiring the impact of photosynthesis in the oxidation and accumulation of the metals, but also in their diagenetic stabilization through microbially mediated organic diagenesis. Results showed that the precursor sediment had high Mn : Fe ratios—values significantly above that typical of the solid Earth, implying kinetic control of facies stacking patterns in the Hotazel Formation. Future work on understanding the paleoredox conditions required to produce certain types of sedimentary rocks might benefit from similar approaches that seek to quantify the convolution of initial sediment composition and the time-dependent properties of diagenetic reactions that can lead to geologically stable, disequilibrium mineral assemblages. This type of approach might also be useful in evaluating the unexpected and common manganese mineralization observed in ancient sedimentary rocks on Mars (Lanza et al., 2014; Stamenković et al., 2018).

ACKNOWLEDGEMENTS

Support for this work was provided by the Simons Foundation Collaboration on the Origins of Life, the Agouron Institute, and David and Lucille Packard Foundation, and a NSF GRFP to KSM. Portions of this research were carried out at the Stanford Synchrotron Radiation Lightsource, SLAC National Accelerator Laboratory, a DOE Office of Science User Facility.

REFERENCES

BEKKER, A., KAUFMAN, A.J., KARHU, J.A., BEUKES, N.J., SWART, Q.D., COETZEE, L.L., AND ERIKSSON, K.A., 2001, Chemostratigraphy of the Paleoproterozoic Duitschland Formation, South Africa: Implications for Coupled Climate Change and Carbon Cycling: American Journal of Science, v. 301, p. 261–285, doi: 10.2475/ajs.301.3.261.

BÉNÉZETH, P., DANDURAND, J.L., and HARRICHOURY, J.C., 2009, Solubility product of siderite (FeCO3) as a function of temperature (25–250 °C): Chemical Geology, v. 265, p. 3–12, doi: 10.1016/j.chemgeo.2009.03.015.

BEUKES, N.J., 1987, Facies relations, depositional environments and diagenesis in a major early Proterozoic stromatolitic carbonate platform to basinal sequence, Campbellrand Subgroup, Transvaal Supergroup, Southern Africa: Sedimentary Geology, v. 54, p. 1–46, doi: 10.1016/0037-0738(87)90002-9.

BEUKES, N.J., 1983, Palaeoenvironmental Setting of Iron-Formations in the Depositional Basin of the Transvaal Supergroup, South Africa, *in* Trendall, A.F. and Morris, R.C., eds., Iron-Formation: Facts and Problems: Developments in Precambrian Geology, Elsevier, Amsterdam, p. 558.

BUTLER, J.E., YOUNG, N.D., and LOVLEY, D.R., 2009, Evolution from a respiratory ancestor to fill syntrophic and fermentative niches: comparative genomics of six Geobacteraceae species: BMC Genomics, v. 10, p. 1–10, doi: 10.1186/1471-2164-10-103.

CAIRNCROSS, B., and BEUKES, N.J., 2013, The Kalahari Manganese Field: the adventure continues: Struik Nature, Cape Town.

CALVERT, S.E., and Pedersen, T.F., 1996, Sedimentary geochemistry of manganese; implications for the environment of formation of manganiferous black shales: Economic Geology, v. 91, p. 36–47, doi: 10.2113/gsecongeo.91.1.36.

CANFIELD, D.E., 1998, A new model for Proterozoic ocean chemistry: Nature, v. 396, p. 450–453, doi: 10.1038/24839.

CONDIE, K.C., 1993, Chemical composition and evolution of the upper continental crust: Contrasting results from surface samples and shales: Chemical Geology, v. 104,

p. 1–37, doi: 10.1016/0009-2541(93)90140-E.

CORNELL, D.H., and SCHÜTTE, S.S., 1995, A volcanic-exhalative origin for the world's largest (Kalahari) Manganese field: Mineralium Deposita, v. 30, p. 146–151, doi: 10.1007/bf00189343.

DUCKWORTH, O.W., and SPOSITO, G., 2005, Siderophore−Manganese(III) Interactions. I. Air-Oxidation of Manganese(II) Promoted by Desferrioxamine B: Environmental Science & Technology, v. 39, p. 6037–6044, doi: 10.1021/es050275k.

ELZINGA, E.J., 2011, Reductive transformation of birnessite by aqueous Mn(II): Environ Sci Technol, v. 45, p. 6366–72, doi: 10.1021/es2013038.

ELZINGA, E.J., and KUSTKA, A.B., 2015, A Mn-54 Radiotracer Study of Mn Isotope Solid–Liquid Exchange during Reductive Transformation of Vernadite (δ-MnO2) by Aqueous Mn(II): Environmental Science & Technology, v. 49, p. 4310–4316, doi: 10.1021/acs.est.5b00022.

EVANS, D.A., BEUKES, N.J., and KIRSCHVINK, J.L., 1997, Low-latitude glaciation in the Palaeoproterozoic era: Nature, v. 386, p. 262–266, doi: 10.1038/386262a0.

EVANS, D., GUTZMER, J., BEUKES, N., and KIRSCHVINK, J., 2001, Paleomagnetic constraints on ages of mineralization in the Kalahari manganese field, South Africa: Economic Geology, v. 96, p. 621–631.

FARQUHAR, J., BAO, H., and THIEMENS, M., 2000, Atmospheric Influence of Earth's Earliest Sulfur Cycle: Science, v. 289, p. 756, doi: 10.1126/science.289.5480.756.

FISCHER, W.W., HEMP, J., and VALENTINE, J.S., 2016, How did life survive Earth's great oxygenation? Current Opinion in Chemical Biology, v. 31, p. 166–178, doi: 10.1016/j.cbpa.2016.03.013.

FROELICH, P.N., KLINKHAMMER, G.P., BENDER, M.L., LUEDTKE, N.A., HEATH, G.R., CULLEN, D., DAUPHIN, P., HAMMOND, D., HARTMAN, B., and MAYNARD, V., 1979, Early oxidation of organic matter in pelagic sediments of the eastern equatorial Atlantic: suboxic diagenesis: Geochimica et Cosmochimica Acta, v. 43, p. 1075–1090, doi: 10.1016/0016-7037(79)90095-4.

GLASBY, G.P., 2006, Manganese: Predominant Role of Nodules and Crusts, *in* Schulz, H.D. and Zabel, M., eds., Marine Geochemistry: Springer Berlin Heidelberg, Berlin, Heidelberg, p. 371–427. https://doi.org/10.1007/3-540-32144-6_11.

GUMSLEY, A.P., CHAMBERLAIN, K.R., BLEEKER, W., SÖDERLUND, U., DE KOCK, M.O., LARSSON, E.R., and BEKKER, A., 2017, Timing and tempo of the Great Oxidation Event: Proceedings of the National Academy of Sciences, v. 114, p. 1811, doi: 10.1073/pnas.1608824114.

GUO, Q., STRAUSS, H., KAUFMAN, A.J., SCHRÖDER, S., GUTZMER, J., WING, B., BAKER, M.A., BEKKER, A., JIN, Q., KIM, S.-T., and FARQUHAR, J., 2009, Reconstructing Earth's surface oxidation across the Archean-Proterozoic transition: Geology, v. 37, p. 399–402, doi: 10.1130/g25423a.1.

GUTZMER, J., and BEUKES, N.J., 1996, Mineral paragenesis of the Kalahari manganese field, South Africa: Ore Geology Reviews, v. 11, p. 405–428.

HEM, J.D., and LIND, C.J., 1983, Nonequilibrium models for predicting forms of precipitated manganese oxides: Geochimica et Cosmochimica Acta, v. 47, p. 2037–2046, doi: 10.1016/0016-7037(83)90219-3.

HERNAN, L., MORALES, J., and TIRADO, J.L., 1986, Relationships between composition and surface properties of the dehydration products of synthetic manganite: Surface and Coatings Technology, v. 27, p. 343–350, doi: 10.1016/0257-8972(86)90074-5.

HOFFMAN, P.F., 2013, The Great Oxidation and a Siderian snowball Earth: MIF-S based correlation of Paleoproterozoic glacial epochs: Chemical Geology, v. 362, p. 143–156, doi: 10.1016/j.chemgeo.2013.04.018.

HOLLAND, H.D., 1984, Chemical Evolution of the Atmosphere and Oceans: Princeton University Press, Princeton, NJ, 582 p.

HOLLAND, H.D., 2006, The oxygenation of the atmosphere and oceans: Philosophical transactions of the Royal Society of London. Series B, Biological sciences, v. 361, p. 903–915, doi: 10.1098/rstb.2006.1838.

JAMES, H.L., 1954, Sedimentary facies of iron-formation: Economic Geology, v. 49, p. 235–293, doi: 10.2113/gsecongeo.49.3.235.

JENSEN, D.L., BODDUM, J.K., TJELL, J.C., and CHRISTENSEN, T.H., 2002, The solubility of rhodochrosite (MnCO3) and siderite (FeCO3) in anaerobic aquatic environments:

Applied Geochemistry, v. 17, p. 503–511, doi: 10.1016/S0883-2927(01)00118-4.

JOHNSON, J.E., SAVALIA, P., DAVIS, R., KOCAR, B.D., WEBB, S.M., NEALSON, K.H., and FISCHER, W.W., 2016a, Real-Time Manganese Phase Dynamics during Biological and Abiotic Manganese Oxide Reduction: Environmental Science & Technology, doi: 10.1021/acs.est.5b04834. http://dx.doi.org/10.1021/acs.est.5b04834.

JOHNSON, J.E., WEBB, S.M., MA, C., and FISCHER, W.W., 2016b, Manganese mineralogy and diagenesis in the sedimentary rock record: Geochimica et Cosmochimica Acta, v. 173, p. 210–231, doi: 10.1016/j.gca.2015.10.027.

JOHNSON, J.E., WEBB, S.M., THOMAS, K., ONO, S., KIRSCHVINK, J.L., and FISCHER, W.W., 2013, Manganese-oxidizing photosynthesis before the rise of cyanobacteria: Proceedings of the National Academy of Sciences of the United States of America, v. 110, p. 11238–11243, doi: 10.1073/pnas.1305530110.

KIRSCHVINK, J.L., GAIDOS, E.J., BERTANI, L.E., BEUKES, N.J., GUTZMER, J., MAEPA, L.N., and STEINBERGER, R.E., 2000, Paleoproterozoic snowball Earth: Extreme climatic and geochemical global change and its biological consequences: Proceedings of the National Academy of Sciences of the United States of America, v. 97, p. 1400–1405.

KNOLL, A.H., and BEUKES, N.J., 2009, Introduction: Initial investigations of a Neoarchean shelf margin-basin transition (Transvaal Supergroup, South Africa): Precambrian Research, v. 169, p. 1–14, doi: 10.1016/j.precamres.2008.10.009.

KOPP, R.E., KIRSCHVINK, J.L., HILBURN, I.A., and NASH, C.Z., 2005, The Paleoproterozoic snowball Earth: A climate disaster triggered by the evolution of oxygenic photosynthesis: Proceedings of the National Academy of Sciences of the United States of America, v. 102, p. 11131–11136, doi: 10.1073/pnas.0504878102.

KOSTKA, J.E., LUTHER, G.W., and NEALSON, K.H., 1995, Chemical and biological reduction of Mn (III)-pyrophosphate complexes: Potential importance of dissolved Mn (III) as an environmental oxidant: Geochimica et Cosmochimica Acta, v. 59, p. 885–894, doi: 10.1016/0016-7037(95)00007-0.

KOTLOSKI, N.J., and GRALNICK, J.A., 2013, Flavin electron shuttles dominate extracellular electron transfer by Shewanella oneidensis: MBio, v. 4, doi: 10.1128/mBio.00553-12. http://mbio.asm.org/content/4/1/e00553-12.full.pdf.

LANTINK, M.L., OONK, P.B.H., FLOOR, G.H., TSIKOS, H., and MASON, P.R.D., 2018, Fe isotopes of a 2.4 Ga hematite-rich IF constrain marine redox conditions around the GOE: Precambrian Research, v. 305, p. 218–235, doi: 10.1016/j.precamres.2017.12.025.

LANZA, N.L., FISCHER, W.W., WIENS, R.C., GROTZINGER, J., OLLILA, A.M., COUSIN, A., ANDERSON, R.B., CLARK, B.C., GELLERT, R., MANGOLD, N., MAURICE, S., LE MOUELIC, S., NACHON, M., SCHMIDT, M., et al., 2014, High manganese concentrations in rocks at Gale crater, Mars: Geophysical Research Letters, v. 41, p. 5755–5763.

LEFKOWITZ, J.P., ROUFF, A.A., and ELZINGA, E.J., 2013, Influence of pH on the Reductive Transformation of Birnessite by Aqueous Mn(II): Environmental Science & Technology, v. 47, p. 10364–10371, doi: 10.1021/es402108d.

LIN, H., SZEINBAUM, N.H., DICHRISTINA, T.J., and TAILLEFERT, M., 2012, Microbial Mn(IV) reduction requires an initial one-electron reductive solubilization step: Geochimica et Cosmochimica Acta, v. 99, p. 179–192, doi: 10.1016/j.gca.2012.09.020.

LINGAPPA, U.F., MONTEVERDE, D.R., MAGYAR, J.S., VALENTINE, J.S., and FISCHER, W.W., 2019, How manganese empowered life with dioxygen (and vice versa): Free Radic Biol Med, v. 140, p. 113–125, doi: 10.1016/j.freeradbiomed.2019.01.036.

LOVLEY, D.R., 1991, Dissimilatory Fe(III) and Mn(IV) reduction: Microbiological Reviews, v. 55, p. 259–287.

LUO, G., ONO, S., BEUKES, N.J., WANG, D.T., XIE, S., and SUMMONS, R.E., 2016, Rapid oxygenation of Earth's atmosphere 2.33 billion years ago: Science Advances, v. 2, doi: 10.1126/sciadv.1600134. http://advances.sciencemag.org/content/advances/2/5/e1600134.full.pdf.

LUTHER, G.W., 2010, The Role of One- and Two-Electron Transfer Reactions in Forming

Thermodynamically Unstable Intermediates as Barriers in Multi-Electron Redox Reactions: Aquatic Geochemistry, v. 16, p. 395–420, doi: 10.1007/s10498-009-9082-3.

MADISON, A.S., TEBO, B.M., MUCCI, A., SUNDBY, B., and LUTHER, G.W., 2013, Abundant Porewater Mn(III) Is a Major Component of the Sedimentary Redox System: Science, v. 341, p. 875–878, doi: 10.1126/science.1241396.

MARGOLIS, S.V., and BURNS, R.G., 1976, Pacific Deep-Sea Manganese Nodules: Their Distribution, Composition, and Origin: Annual Review of Earth and Planetary Sciences, v. 4, p. 229–263, doi: 10.1146/annurev.ea.04.050176.001305.

MAYNARD, J.B., 2010, The Chemistry of Manganese Ores through Time: A Signal of Increasing Diversity of Earth-Surface Environments: Economic Geology, v. 105, p. 535–552, doi: 10.2113/gsecongeo.105.3.535.

MILLERO, F.J., SOTOLONGO, S., and IZAGUIRRE, M., 1987, The oxidation kinetics of Fe (II) in seawater: Geochimica et Cosmochimica Acta, v. 51, p. 793–801.

MOREL, F.M.M., and HERING, J.G., 1993, Principles and Applications of Aquatic Chemistry: Wiley. https://books.google.com/books?id=Rs31PfkeBaIC.

MORGAN, J.J., 2005, Kinetics of reaction between O2 and Mn(II) species in aqueous solutions: Geochimica et Cosmochimica Acta, v. 69, p. 35–48, doi: 10.1016/j.gca.2004.06.013.

MUCCI, A., 2004, The Behavior of Mixed Ca–Mn Carbonates in Water and Seawater: Controls of Manganese Concentrations in Marine Porewaters: Aquatic Geochemistry, v. 10, p. 139–169, doi: 10.1023/B:AQUA.0000038958.56221.b4.

MYERS, C.R., and NEALSON, K.H., 1988, Microbial reduction of manganese oxides: Interactions with iron and sulfur: Geochimica et Cosmochimica Acta, v. 52, p. 2727–2732, doi: 10.1016/0016-7037(88)90041-5.

NAVROTSKY, A., MA, C., LILOVA, K., and BIRKNER, N., 2010, Nanophase Transition Metal Oxides Show Large Thermodynamically Driven Shifts in Oxidation-Reduction Equilibria: Science, v. 330, p. 199–201, doi: 10.1126/science.1195875.

NEL, C.J., BEUKES, N.J., and DE VILLERS, J.P.R., 1986, The Mamatwan manganese mine of the Kalahari Manganese Field, *in* Anhaeusser, C.R. and Maske, S., eds., Mineral Deposits of Southern Africa: Geological Society of South Africa.

OKITA, P.M., MAYNARD, J.B., SPIKER, E.C., and FORCE, E.R., 1988, Isotopic evidence for organic matter oxidation by manganese reduction in the formation of stratiform manganese carbonate ore: Journal Name: Geochimica et Cosmochimica Acta; (USA); Journal Volume: 52:11, p. Medium: X; Size: Pages: 2679-2685.

OLDHAM, V.E., OWINGS, S.M., JONES, M.R., TEBO, B.M., and LUTHER, G.W., 2015, Evidence for the presence of strong Mn(III)-binding ligands in the water column of the Chesapeake Bay: Marine Chemistry, v. 171, p. 58–66, doi: 10.1016/j.marchem.2015.02.008.

POST, J.E., 1999, Manganese oxide minerals: Crystal structures and economic and environmental significance: Proceedings of the National Academy of Sciences, v. 96, p. 3447–3454, doi: 10.1073/pnas.96.7.3447.

POSTMA, D., 1985, Concentration of Mn and separation from Fe in sediments—I. Kinetics and stoichiometry of the reaction between birnessite and dissolved Fe(II) at 10°C: Geochimica et Cosmochimica Acta, v. 49, p. 1023–1033, doi: 10.1016/0016-7037(85)90316-3.

POSTMA, D., and APPELO, C.A.J., 2000, Reduction of Mn-oxides by ferrous iron in a flow system: column experiment and reactive transport modeling: Geochimica et Cosmochimica Acta, v. 64, p. 1237–1247, doi: 10.1016/S0016-7037(99)00356-7.

RAISWELL, R., and FISHER, Q.J., 2000, Mudrock-hosted carbonate concretions: a review of growth mechanisms and their influence on chemical and isotopic composition: Journal of the Geological Society, v. 157, p. 239–251, doi: 10.1144/jgs.157.1.239.

RICHARDSON, D.J., BUTT, J.N., FREDRICKSON, J.K., ZACHARA, J.M., SHI, L., EDWARDS, M.J., WHITE, G., BAIDEN, N., GATES, A.J., MARRITT, S.J., and CLARKE, T.A., 2012, The "porin-cytochrome" model for microbe-to-mineral electron transfer: Mol Microbiol, v. 85, p. 201–12, doi: 10.1111/j.1365-2958.2012.08088.x.

ROBIE, R.A., HUEBNER, J.S., and HEMINGWAY, B.S., 1995, Heat capacities and thermodynamic properties of braunite (Mn7SiO12) and rhodonite (MnSiO3): American Mineralogist, v. 80, p. 560–575, doi: 10.2138/am-1995-5-616.

SCHAEFER, M.V., HANDLER, R.M., and SCHERER, M.M., 2017, Fe(II) reduction of pyrolusite (β-MnO 2) and secondary mineral evolution: Geochemical Transactions, v. 18, p. 1–11, doi: 10.1186/s12932-017-0045-0.

SCHNEIDERHAN, E.A., GUTZMER, J., STRAUSS, H., MEZGER, K., and BEUKES, N.J., 2006, The chemostratigraphy of a Paleoproterozoic MnF-BIF succession - the Voëlwater Subgroup of the Transvaal Supergroup in Griqualand West, South Africa: South African Journal of Geology, v. 109, p. 63–80.

SHAMPINE, L.F., and REICHELT, M.W., 1997, The MATLAB ODE Suite: SIAM J. Sci. Comput., v. 18, p. 1–22, doi: 10.1137/s1064827594276424.

SIEBECKER, M., MADISON, A.S., and LUTHER, G.W., 2015, Reduction Kinetics of Polymeric (Soluble) Manganese (IV) Oxide (MnO2) by Ferrous Iron (Fe2+): Aquatic Geochemistry, v. 21, p. 143–158, doi: 10.1007/s10498-015-9257-z.

STAMENKOVIĆ, V., WARD, L.M., MISCHNA, M., and FISCHER, W.W., 2018, O2 solubility in Martian near-surface environments and implications for aerobic life: Nature Geoscience, v. 11, p. 905–909, doi: 10.1038/s41561-018-0243-0.

STERNBECK, J., 1997, Kinetics of rhodochrosite crystal growth at 25°C: The role of surface speciation: Geochimica et Cosmochimica Acta, v. 61, p. 785–793, doi: 10.1016/S0016-7037(96)00379-1.

SUMNER, D.Y., and GROTZINGER, J.P., 1996, Were kinetics of Archean calcium carbonate precipitation related to oxygen concentration? Geology, v. 24, p. 119–122, doi: 10.1130/0091-7613(1996)024<0119:wkoacc>2.3.co;2.

TAKASHIMA, T., HASHIMOTO, K., and NAKAMURA, R., 2012, Mechanisms of pH-Dependent Activity for Water Oxidation to Molecular Oxygen by MnO2 Electrocatalysts: Journal of the American Chemical Society, v. 134, p. 1519–1527, doi: 10.1021/ja206511w.

TANG, Y.J., MEADOWS, A.L., and KEASLING, J.D., 2007, A kinetic model describing Shewanella oneidensis MR-1 growth, substrate consumption, and product secretion: Biotechnology and Bioengineering, v. 96, p. 125–133, doi: 10.1002/bit.21101.

TAYLOR, S.R., and MCLENNAN, S.M., 1995, The Geochemical Evolution of the Continental Crust: Reviews of Geophysics, v. 33, p. 241–265.

TSIKOS, H., BEUKES, N.J., MOORE, J.M., and HARRIS, C., 2003, Deposition, Diagenesis, and Secondary Enrichment of Metals in the Paleoproterozoic Hotazel Iron Formation, Kalahari Manganese Field, South Africa: Economic Geology, v. 98, p. 1449–1462, doi: 10.2113/gsecongeo.98.7.1449.

TSIKOS, H., MATTHEWS, A., EREL, Y., and MOORE, J.M., 2010, Iron isotopes constrain biogeochemical redox cycling of iron and manganese in a Palaeoproterozoic stratified basin: Earth and Planetary Science Letters, v. 298, p. 125–134, doi: 10.1016/j.epsl.2010.07.032.

TSIKOS, H., and MOORE, J.M., 1997, Petrography and geochemistry of the Paleoproterozoic Hotazel Iron-Formation, Kalahari manganese field, South Africa; implications for Precambrian manganese metallogenesis: Economic Geology, v. 92, p. 87–97, doi: 10.2113/gsecongeo.92.1.87.

VAN CAPPELLEN, P., and WANG, Y., 1996, Cycling of iron and manganese in surface sediments; a general theory for the coupled transport and reaction of carbon, oxygen, nitrogen, sulfur, iron, and manganese: American Journal of Science, v. 296, p. 197–243, doi: 10.2475/ajs.296.3.197.

VEIZER, J., HOEFS, J., LOWE, D.R., and THURSTON, P.C., 1989, Geochemistry of Precambrian carbonates: II. Archean greenstone belts and Archean sea water: Geochim Cosmochim Acta, v. 53, p. 859–71.

VILLINSKI, J.E., O'DAY, P.A., CORLEY, T.L., and CONKLIN, M.H., 2001, In Situ Spectroscopic and Solution Analyses of the Reductive Dissolution of MnO2 by Fe(II): Environmental Science & Technology, v. 35, p. 1157–1163, doi: 10.1021/es001356d.

VILLINSKI, J.E., SAIERS, J.E., and CONKLIN, M.H., 2003, The Effects of Reaction-Product Formation on the Reductive Dissolution of MnO2 by Fe(II): Environmental Science & Technology, v. 37, p. 5589–5596, doi: 10.1021/es034060r.

WAYCHUNAS, G.A., 1991, Crystal Chemistry of Oxides and Oxyhydroxides, *in* Lindsay, D.H., ed., Oxide Minerals: Petrologic and Magnetic Significance: Reviews in Mineralogy, Mineralogical Society of America, p. 55.

WEBB, S.M., 2006, SMAK: Sam's Microprobe Analysis Kit: Stanford Synchrotron

Radiation Laboratory, Menlo Park, CA.

WEBB, S.M., DICK, G.J., BARGAR, J.R., and TEBO, B.M., 2005, Evidence for the presence of Mn(III) intermediates in the bacterial oxidation of Mn(II): Proceedings of the National Academy of Sciences, v. 102, p. 5558–5563, doi: 10.1073/pnas.0409119102.

XU, T., APPS, J.A., and PRUESS, K., 2004, Mineral sequestration of carbon dioxide in a sandstone–shale system: Chemical Geology, v. 217, p. 295–318, doi: 10.1016/j.chemgeo.2004.12.015.